Journal of *Marine Science and Engineering*

MDPI

Article

Numerical and Experimental Investigation of a Ducky Wave Energy Converter and Its Impact on Floating Ocean Wind Turbines

Tao Tao [1,†], Yu Dong [2,†], Xinran Guo [1], Shi Liu [1,3], Yichen Jiang [2,4,*] and Zhiming Yuan [5,*]

[1] China Southern Power Grid Technology Co., Ltd., Guangzhou 510080, China; taot0804@163.com (T.T.); g18820101803@163.com (X.G.); 13925041516@139.com (S.L.)
[2] School of Naval Architecture and Ocean Engineering, Dalian University of Technology, Dalian 116024, China; dy@mail.dlut.edu.cn
[3] National Institute of Guangdong Advanced Energy Storage Co., Ltd., Guangzhou 510410, China
[4] Dalian Technical Shenzhen Research Institute, Shenzhen 518063, China
[5] Department of Naval Architecture, Ocean and Marine Engineering, University of Strathclyde, Glasgow G4 0LZ, UK
* Correspondence: ycjiang@dlut.edu.cn (Y.J.); zhiming.yuan@strath.ac.uk (Z.Y.)
† These authors contributed equally to this work.

Abstract

The ocean represents a vast reservoir of energy. To address the issue of wave-induced motion in floating wind farms—particularly pitch motion—while harnessing the otherwise dissipated wave energy for power generation, this study proposes an integrated solution. Specifically, a duck-shaped wave energy converter incorporating mooring and power take-off systems is introduced. By combining computational fluid dynamics with experimental fluid dynamics methodologies, the performance of the device was systematically evaluated and its key parameters—including floating attitude, power take-off damping, and mooring configuration—were optimized. Furthermore, results indicate that deploying the duck-shaped converter around the periphery of a wind farm can reduce the wave-induced motion amplitude of the floating wind turbine platform by more than 70%, especially in terms of pitch motion, thereby significantly improving the operational efficiency and structural stability of the wind turbines.

Keywords: wave energy converter; PTO system; RAOs; generation power; efficiency

Received: 24 June 2025
Revised: 1 August 2025
Accepted: 6 August 2025
Published: 8 August 2025

Citation: Tao, T.; Dong, Y.; Guo, X.; Liu, S.; Jiang, Y.; Yuan, Z. Numerical and Experimental Investigation of a Ducky Wave Energy Converter and Its Impact on Floating Ocean Wind Turbines. *J. Mar. Sci. Eng.* **2025**, *13*, 1527. https://doi.org/10.3390/jmse13081527

1. Introduction

1.1. Background

Global energy demand continues to rise significantly with societal and technological development [1], leading to a dramatic increase in fossil fuel consumption [2]. However, this reliance poses severe challenges: ozone layer depletion, climate change, and environmental pollution. Notably, atmospheric CO_2 concentrations have surged from 280 ppm pre-industrial to 390 ppm today [3]. Compounding this issue, fossil fuels are finite and non-renewable, raising concerns about long-term energy security [4].

Renewable energy sources offer a critical pathway towards sustainability, characterized by near-zero net emissions, low costs, and environmental benefits [5–7]. Among these, ocean energy holds immense potential due to its vast reserves and high energy flow density (2~3 kW/m^2), exceeding that of solar (0.1~0.2 kW/m^2) and wind energy (0.4~0.6 kW/m^2) [8]. Ocean energy encompasses various forms, including wave, tidal

current, salinity gradient, and thermal gradient energy [9]. Wave energy, defined as the sum of kinetic and potential energy in ocean waves [10], stands out as particularly promising. It boasts advantages such as low transmission loss [11], good predictability [12], periodicity, and minimal environmental interference [8]. Global estimates suggest immense wave energy resources, with approximately 3 TW available (excluding low-density areas < 1 kW/m) [13], an average of about 2.11 TW along coastlines [14], and a projected annual potential of 29,500 TWh [15,16]. Consequently, wave energy is recognized as a key contributor to decarbonization and energy security, reflected in ambitious targets like the OES goal of over 300 GW installed capacity by 2050 [17]. Market projections further underscore this potential, forecasting significant growth from USD 500 million (2022) to USD 2.1 billion (2030) at a 20.2% CAGR, and reaching USD 120 million by 2029 with a 21.1% CAGR.

Despite this significant potential and growing interest, the efficient and cost-effective conversion of wave energy into usable electricity remains a critical challenge [18]. Current research predominantly focuses on electrical energy conversion [18], but broader exploration of optimal utilization pathways is needed to unlock its full contribution to the energy mix.

1.2. Research Advances and Analyses

The high cost of wave energy generation remains a formidable barrier to the commercial deployment of Wave Energy Converters (WECs). These costs primarily stem from device construction and electricity transmission. To address these challenges, research has pursued two main avenues: optimizing individual WEC designs for enhanced performance and cost reduction and exploring synergistic integration with other marine structures or renewable energy sources. The latter includes incorporating WECs (e.g., 'Salter Cam') into breakwaters or co-locating them with offshore wind farms to share infrastructure costs like transmission cables and substations [19–22].

Among the diverse WEC archetypes developed over centuries [23–25], the 'Salter Duck' (or nodding duck), conceived by Professor Salter, has long been recognized for its high theoretical energy capture efficiency under regular waves [26–28]. Subsequent research has focused on optimizing its geometry [27,28], connection mechanisms [29], and understanding its performance under various wave conditions (regular vs. irregular) [29–31]. Full-scale component design has also been explored [32]. Extensions of the concept, like the WEPTOS device connecting multiple ducks to a common shaft, have been experimentally investigated, although often focusing on mechanical power without full PTO integration or grid connection analysis [33]. Recent CFD studies have examined wave interaction and energy extraction for the Salter Duck configuration [34].

However, the translation of Salter Duck's promise into a practical, deep-water floating WEC solution faces significant research gaps in the existing literature. Much of the foundational understanding relies on simplified 2D numerical simulations or theoretical analyses [27,28,30,31,34], which inherently neglect crucial 3D effects present in realistic device geometries. Furthermore, experimental validation has frequently employed fixed shaft constraints [29,33], anchoring the device conceptually to near-shore applications with expensive foundation requirements and overlooking the vast, untapped wave energy resource of the deep ocean. Crucially, there is a notable scarcity of studies investigating the fully coupled dynamics of a 3D, freely floating Salter Duck WEC system that integrates both its mooring system and a realistic Power Take-Off (PTO) mechanism under operational wave conditions. This gap directly impedes a comprehensive assessment of its true power generation potential and overall efficiency in the floating configuration envisioned for deep-water deployment. Consequently, robust performance data and validated models for such a holistic floating Salter Duck system remain largely absent.

Beyond electricity generation, WECs inherently act as wave attenuators during energy extraction [35]. This secondary function has motivated significant research into their integration with offshore wind farms, not only for cost-sharing benefits [19,20,22] but also for enhancing wind turbine operation. Studies indicate that strategically placed WECs can effectively reduce wave-induced platform motions (particularly pitch), thereby improve the seakeeping performance and potentially extend the operational window of Floating Offshore Wind Turbines (FOWTs) [36,37]. The concept of integrating WECs within FOWT farms to boost overall energy yield and reliability is thus gaining considerable traction [19,21,22]. Building directly upon this established potential for synergy, our work proposes a specific, optimized configuration: deploying a peripheral row of modified roll-type WECs around a floating wind farm. This approach explicitly leverages their dual function—simultaneous energy capture and wave absorption—to provide enhanced protection for the wind farm while enabling significant cost reduction through shared transmission infrastructure.

1.3. Research Content and Contributions

Building upon the challenge of improving wave energy conversion efficiency and cost-effectiveness, as identified in the Section 1.1, this study aims to comprehensively investigate and enhance the performance of a modified floating roll-type WEC based on the 'nodded duck' concept. Furthermore, it seeks to explore the potential for synergistic integration of this WEC with offshore wind farms to reduce overall energy production costs. The overarching aim is supported by the following specific objectives:

To establish and validate a fully coupled dynamic model of the mooring-PTO-WEC system for a realistic performance assessment of the modified floating roll-type WEC based on towing tank experiments. To systematically evaluate the hydrodynamic performance of the modified floater under key design and environmental parameters, including axial depth, heel angle, and wave incident angle, through frequency-domain analysis. To apply a novel qualitative method for efficiency analysis of the floater based on Response Amplitude Operator (RAO) curves. To quantify the power generation capability and efficiency of the device by determining the relationship between optimal PTO damping and wave period, and by evaluating performance under irregular wave conditions, including directional effects. To investigate the optimal operational parameters—such as equivalent damping, power output, and efficiency—under variations in axial depth, heel angle, and wave incident angle.

Additionally, propose and conceptually evaluate a novel integrated system that combines the modified roll-type WEC, breakwaters, and Floating offshore Wind Turbines (FOWT), as shown in Figure 1. The objective is to demonstrate the dual functionality of the WEC array—namely, electricity generation and wave attenuation and significantly reduce the overall cost of offshore renewable energy systems. Furthermore, this integration aims to enhance the operational safety of the wind farm by mitigating wave loads and platform motion.

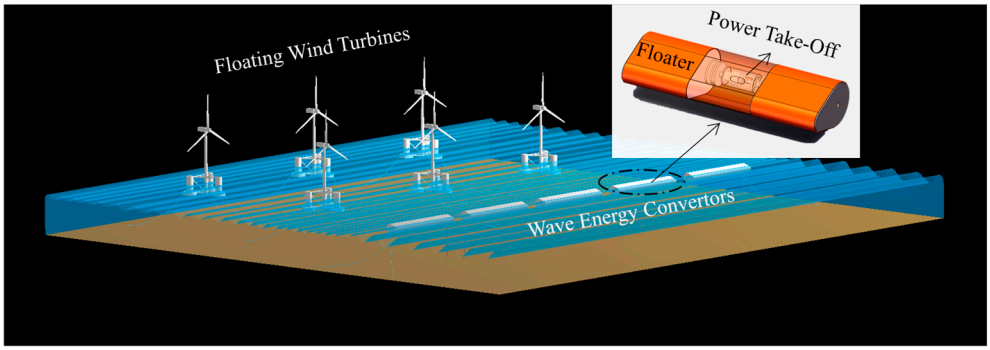

Figure 1. The WEC positioned upstream of the FOWT to mitigate the FOWT's wave motion.

2. Numerical Model

In this study, the software, AQWA R15.0, is employed to analyze the hydrodynamic performance of the roll-type WEC in the frequency domain, as well as its motion response and mooring forces in the time domain. The simulation assumes that the fluid is inviscid, irrotational, and incompressible. The velocity potential at any point in the flow field satisfies the Laplace equation. Once the boundary conditions are defined, the velocity potential of the entire flow field can be determined. Based on the Lagrange integral, the fluid pressure field can then be calculated, and the hydrodynamic forces acting on the WEC body are obtained by integrating the pressure over the wetted surface. Finally, assuming the WEC device behaves as a rigid body, its motion equations are derived according to Newton's second law.

2.1. Frequency Domain Hydrodynamic Model

The hydrodynamic model established in the frequency domain is illustrated in Figure 2. Figure 2a shows the geometric model and the Cartesian coordinate system, while Figure 2b presents the mesh discretization. The device geometry is an improved version of the Salter Cam, featuring a pear-shaped contour with a small anterior beak and a large posterior spine, as depicted in Figure 2a. The device oscillates vertically around the axis located at the posterior spine under the combined influence of the wave moment and the restoring moment. The main geometric and operational parameters of the device are summarized in Table 1. This numerical model utilized a scaled-down model with a geometric scale ratio of 1:25.

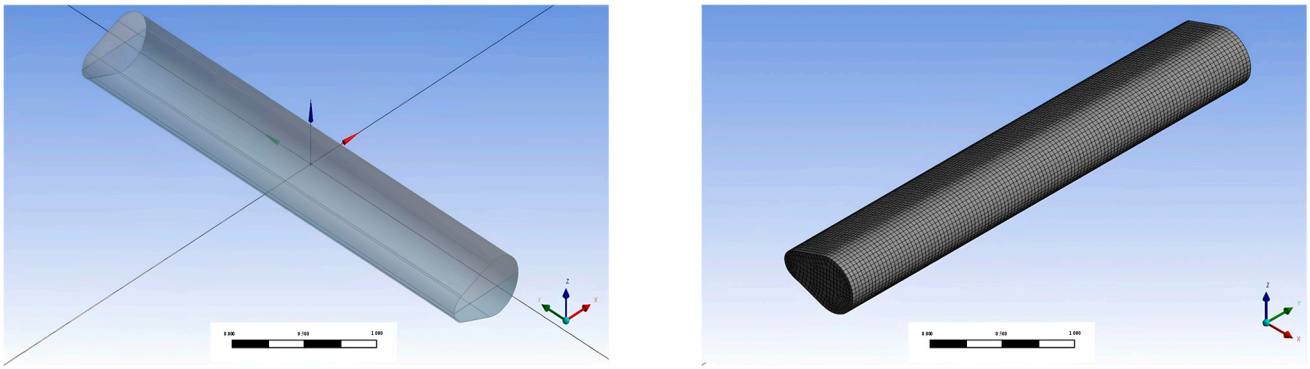

(**a**) (**b**)

Figure 2. Hydrodynamic model: (**a**) Geometric model; (**b**) Grid division.

Table 1. Main parameters of device.

Parameter	Size
Length (m)	3.600
Wide (m)	0.618
Beak radius (m)	0.103
Spine radius (m)	0.206
Draft (m)	0.206
Mass (kg)	331
Moment of inertia I_{xx} (kg·m^2)	356
Moment of inertia I_{yy} (kg·m^2)	11
Moment of inertia I_{zz} (kg·m^2)	365

The motion equation of the device in the frequency domain is:

$$\left[-\omega^2(M+\Delta M(\omega))-i\omega B+C\right]x(\omega)=F(\omega) \quad (1)$$

where M is the mass matrix of the device, ΔM as the added mass matrix, B is the damping matrix, C is the stiffness matrix, F is the wave force [38].

2.2. Time-Domain Coupled Response Model

The time-domain coupled response analysis model with four mooring cables is shown in Figure 3. The fairlead hole is located at the center of the posterior spine on both sides, and the anchor is located on the sea floor. The mooring parameters in the numerical model are set as shown in Table 2.

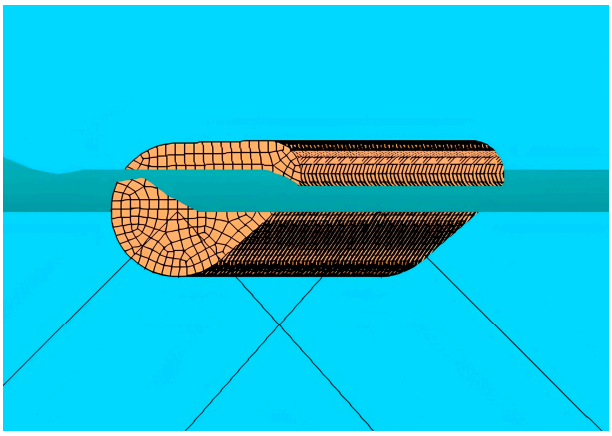

Figure 3. Time-domain coupling response model.

Table 2. Mooring parameters.

Mooring Line Serial	Fairlead Position	Anchor Position
1	(0.0, 1.8, 0.0)	(3.5, 2.5, −3.7)
2	(0.0, 1.8, 0.0)	(−3.5, 2.5, −3.7)
3	(0.0, 1.8, 0.0)	(3.5, −2.5, −3.7)
4	(0.0, 1.8, 0.0)	(−3.5, −2.5, −3.7)

The time-domain motion equation of the device is:

$$(M + \Delta M)\ddot{x}(t) + \int_0^t K(t-\tau)x(\tau)d\tau + Cx(t) = F_1(t) + F_T(t) \quad (2)$$

where M is the mass of the object. ΔM is the added mass, which is often related to the inertial effects of the fluid. $K(t-\tau)$ is the delay function, representing the radiation damping effects on the object. This delay function is typically obtained by the inverse Fourier transform of the radiation damping. C is the damping coefficient. F_1 is the first-order wave force, caused by the waves, F_T is the mooring force [38].

3. Frequency Domain Results

3.1. Frequency Domain Characteristics

Through frequency domain analysis, the added mass, radiation damping coefficient, wave force, and RAOs of the floater can be obtained, which provides a basis for the subsequent time-domain coupled dynamic response calculations. When the device is in static equilibrium in still water, the heel angle is 0°, the axial depth is 0 mm, the draft is 0.206 m, and the coordinates of the center of mass are (−0.076, 0, −0.035). The analyzed wave frequency range is 0.2–1.4 Hz, and the wave incident angle is set to 0°.

The first-order wave forces (moments) in the sway, surge, heave, roll, pitch, and yaw directions are presented in Figure 4. As shown, the wave loads in the sway, heave, and

roll directions are relatively large, whereas the wave loads in the other three directions are nearly zero. This is because the incident wave angle is aligned with the positive X-axis. The roll wave moment initially increases with the wave period, then decreases, and eventually stabilizes at a lower value. The maximum roll wave moment reaches 1272.7694 Nm at a wave frequency corresponding to a frequency of 1.031 Hz.

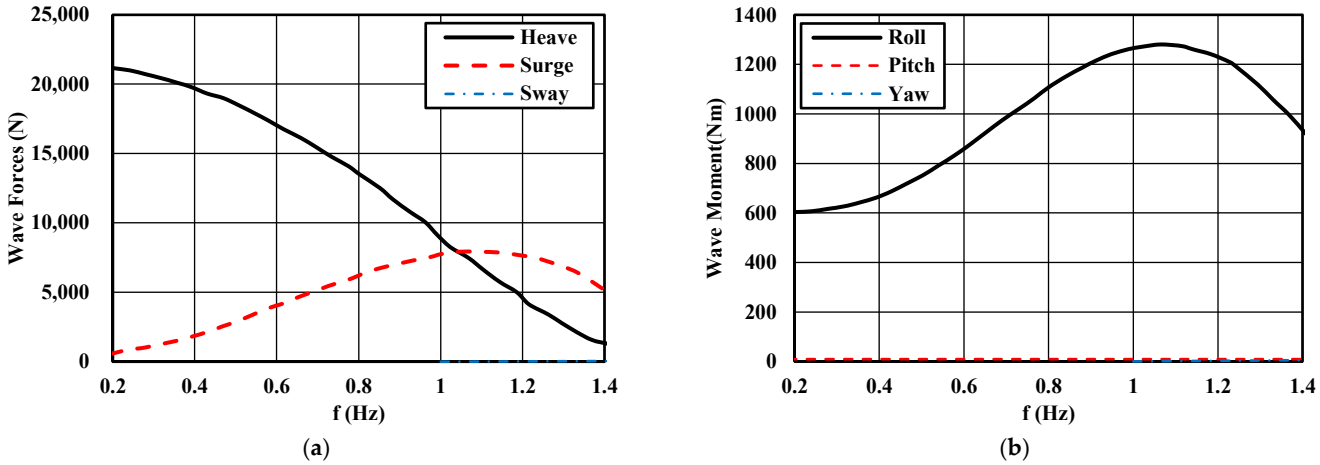

Figure 4. First-order wave force: (**a**) Sway, heave, and surge wave forces; (**b**) Yaw, roll and pitch wave moments.

Figure 5 shows that the sway, heave, and roll RAOs are significantly large, while there is virtually no motion response in the other three degrees of freedom, as the wave forces in those directions are nearly zero. The heave RAO generally increases initially, then decreases, and eventually stabilizes at a value of 1. The heave RAO exhibits two peaks: the main peak is caused by resonance, and the secondary peak results from the coupling between roll and heave motions. The roll RAO first increases and then decreases, reaching its maximum at a wave frequency of 0.945 Hz, which is attributed to the occurrence of roll resonance.

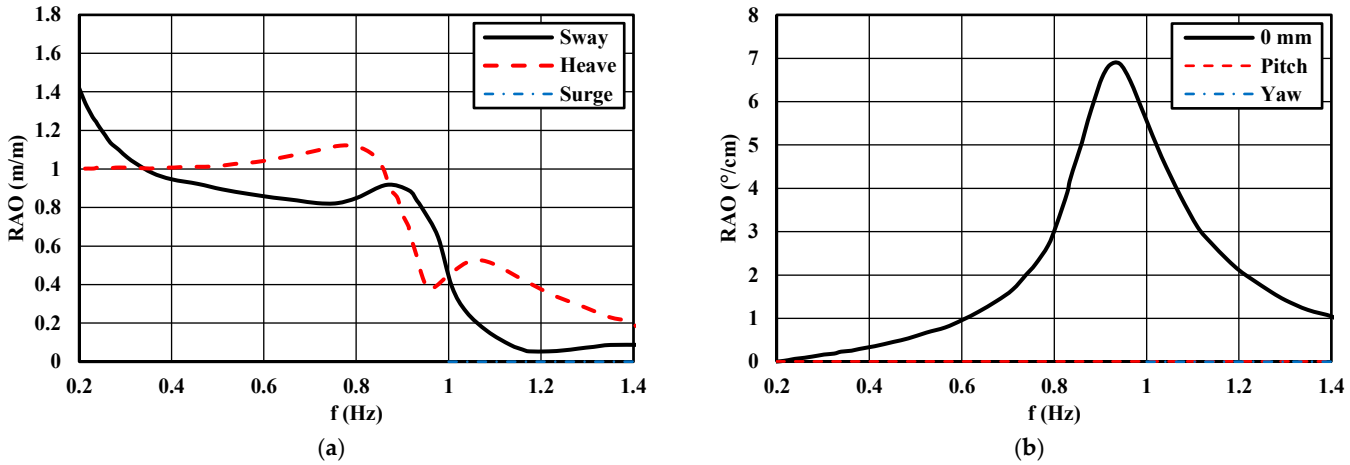

Figure 5. RAOs of the floater: (**a**) Sway, heave and surge RAOs; (**b**) Yaw, roll and pitch RAOs.

3.2. Methods for Evaluating Conversion Efficiency

The focus of this paper is a roll-type WEC, which primarily converts wave energy into mechanical energy associated with roll motion, and subsequently transforms this mechanical energy into electrical energy through the PTO system. Therefore, the key interest lies in the roll motion response. Within the resonance region, the floater exhibits a strong roll response, indicating a greater potential for wave energy absorption. Consequently, the area

of the resonance region is proposed as an indicator for evaluating the conversion efficiency. Specifically, a larger resonance region corresponds to higher mechanical energy in roll motion and improved efficiency in converting wave energy into roll mechanical energy. In this study, the resonance region is defined as the frequency range where the motion response exceeds two-thirds of the peak value, as illustrated in Figure 6. The parameters f1 and f2 denote the minimum and maximum frequencies (or periods) within this resonance region. The term "bandwidth" refers to the difference between f2 and f1 and is used to quantify the width of the resonance region.

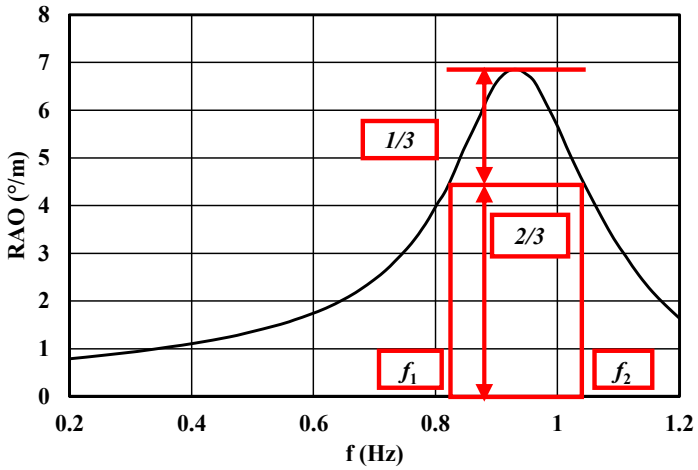

Figure 6. Division of resonance region.

If the PTO system is further considered, a large bandwidth of the WEC body would help minimize the negative impact from the PTO system. Therefore, bandwidth is proposed as an evaluation criterion for the conversion efficiency of the PTO system. This implies that a wider bandwidth corresponds to higher efficiency in converting roll mechanical energy into electrical energy. In the preliminary design phase, this method can be used to qualitatively assess the conversion efficiency of the WEC, facilitating performance improvements and reducing computational effort, thereby decreasing the time cost of the preliminary design. The power generation and efficiency of the device will be quantitatively calculated in the time domain at a later stage, which will verify the reliability of the analytical approach.

3.3. Effect of Axial Depth in Frequency Domain

The axial depth of the device is defined as the vertical distance between the still water surface and the symmetric plane of the floater, with the axis of rotation located in this plane, as illustrated in Figure 7. A desired axial depth can be achieved by adjusting the ballast block in the WEC. To examine the influence of axial depth on system behavior, numerical simulations are performed for axial depths of 0, 10, 20, 40, 50, 60, 70, and 80 mm, under a heel angle of 0° and a wave incident angle of 0°.

Figure 8 shows that the roll wave moment consistently decreases with increasing axial depth. This is primarily because an increase in axial depth reduces the roll arm, thereby leading to a decrease in the roll wave moment. At small wavelengths, the roll wave moment exhibits minimal variation with axial depth, whereas at large wavelengths, the effect of axial depth on the roll wave moment becomes more pronounced. The peak value of the roll wave moment is highly sensitive to changes in axial depth, while the natural period corresponding to this peak remains largely unaffected.

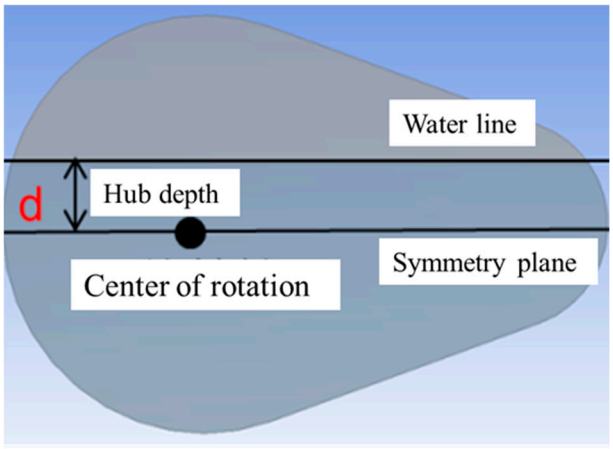

Figure 7. Definition of axial depth of the device.

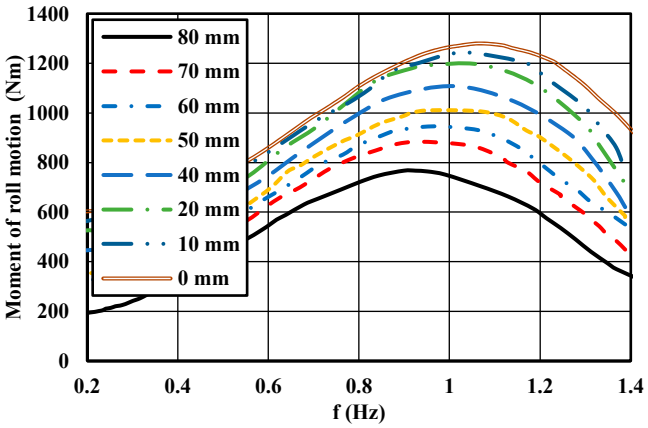

Figure 8. Roll wave moment under different axial depths.

Figure 9 illustrates that the maximum roll moment decreases as the axial depth increases. As shown in the figure, when the axial depth ranges from 0 to 40 mm, the maximum roll wave moment decreases linearly with a reduction rate of 4.25 Nm/mm. In the range of 40 to 70 mm, the decrease remains approximately linear, with an increased reduction rate of 7.27 Nm/mm. When the axial depth is between 70 and 80 mm, the roll wave moment decreases at a significantly higher rate of 11.68 Nm/mm. This indicates that the fastest reduction in roll wave moment occurs in the 70–80 mm axial depth range, followed by the 40–70 mm range, while the slowest reduction is observed between 0 and 40 mm.

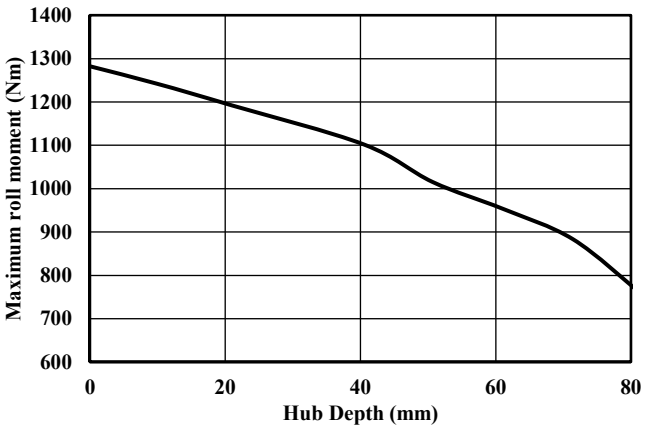

Figure 9. Maximum roll moment at different axial depths.

Figure 10 presents the roll motion RAO in the vicinity of the natural frequency under varying axial depths. At both large and small wavelengths, the roll RAO values are relatively low and exhibit minimal sensitivity to axial depth, as the system operates outside the resonance region. When the axial depth ranges from 0 to 70 mm, the peak roll RAO remains nearly constant, varying between 7.0 and 7.5 deg/cm, with a corresponding natural period range of 1.0 to 1.1 s. This indicates that within this axial depth range, the peak RAO and natural period are scarcely influenced by changes in axial depth. However, when the axial depth increases from 70 to 80 mm, a significant decrease in the peak roll RAO is observed, dropping from 6.8 deg/cm to 4.6 deg/cm. This reduction is attributed to the substantial decline in roll wave moment, as illustrated in Figure 8.

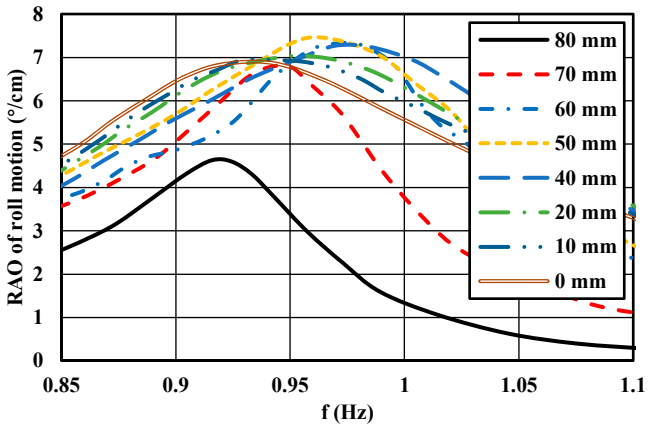

Figure 10. RAO of roll motion in the vicinity of the natural frequency with different axial depths.

The peak value of the roll RAO attains its maximum at an axial depth of 60 mm, as illustrated in Figure 11. The reduction in the peak value is primarily attributed to a significant decrease in the wave force. The corresponding resonance period initially decreases and then increases due to the variation in roll stiffness caused by changes in the wetted surface, reaching its minimum at an axial depth of 40 mm.

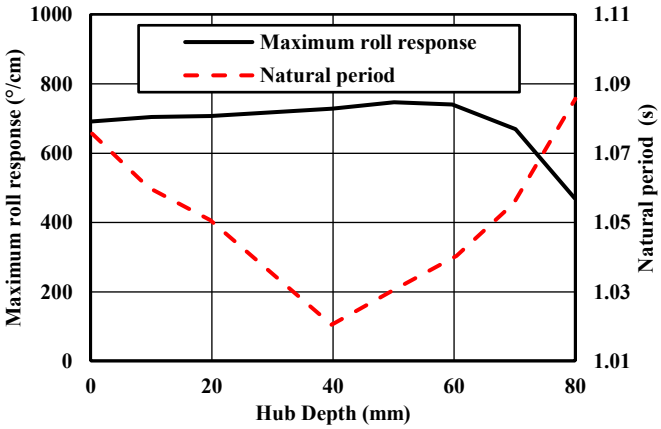

Figure 11. Maximum roll RAO and natural period at different axial depths.

The area of the resonance region reaches its maximum at an axial depth of 20 mm, as shown in Figure 12. This indicates that the roll mechanical energy of the WEC is highest at this depth, and the conversion efficiency from wave energy to roll mechanical energy is also the greatest. When the axial depth ranges from 0 to 40 mm, the resonance region area remains relatively large with minimal variation, mainly between 1.2 and 1.4. This suggests that the device absorbs more wave energy within this range, and the conversion process is efficient. For axial depths from 40 to 80 mm, the area decreases rapidly due to a significant

reduction in the roll wave moment, implying a sharp decline in conversion efficiency. When the axial depth is between 0 and 20 mm, the bandwidth of the resonance region remains constant, indicating stable conversion efficiency of the PTO system. However, for axial depths from 20 to 80 mm, the bandwidth decreases as the axial depth increases, which reflects a reduction in the PTO system's conversion efficiency.

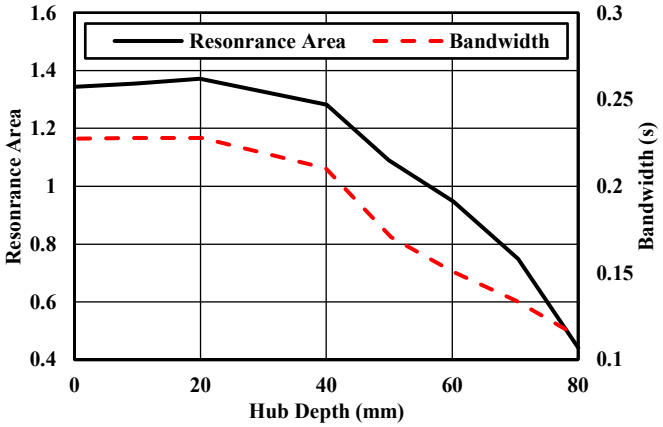

Figure 12. Area and bandwidth of the resonance region under different axial depths.

3.4. Effect of Heel Angle in Frequency Domain

The heel angle of the WEC is defined as the angle between the still water surface and the symmetric plane of the device in still water, as illustrated in Figure 13. The desired heel angle can be achieved by adjusting the center of gravity of the WEC or the mooring pre-tension force. To investigate the influence of heel angle on device performance, the heel angle, axial depth, and wave incident angle are set to 0°, 10°, 20°, and 30°; 0 mm; and 0°, respectively.

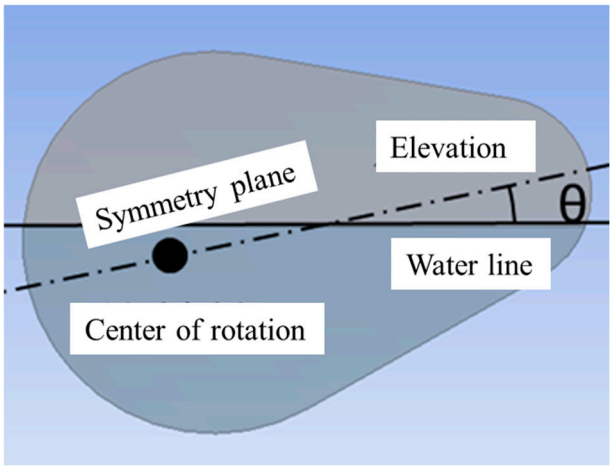

Figure 13. Definition of heel angle of floater.

Figure 14 presents that under different heel angles, the roll wave moment changes with the period roughly the same trend. As the period increases, the roll wave moment first increases, then decreases, and finally reaches a plateau. When the heel angle is from 10 to 30°, the maximum value of the roll wave moment decreases rapidly. This is mainly because the center of wet surface moves towards the back spine, which reduces the roll arm, resulting in a reduction of the roll wave moment.

At a heel angle of 30°, the roll RAO exhibits two distinct peaks, as illustrated in Figure 15. The primary peak is caused by resonance, while the secondary peak results from the coupling between roll and heave motions. The peak value of the roll RAO reaches its

maximum at a heel angle of 20°, indicating that an appropriate increase in heel angle can enhance the roll motion response. However, at larger heel angles, the roll motion response decreases due to reduced wave loading. The roll natural period increases with the heel angle. This phenomenon occurs because the area moment of the waterplane decreases as the heel angle increases, leading to a reduction in the metacentric height and roll stiffness.

Figure 16 shows that the area of the resonance region first increases and then decreases with the heel angle, reaching its maximum at 20°. This indicates that the conversion efficiency from wave energy to roll mechanical energy is highest at a heel angle of 20°. As the heel angle increases, the bandwidth of the resonance region decreases, suggesting that higher heel angles lead to lower PTO conversion efficiency. Overall, the WEC exhibits higher efficiency at heel angles of 0°, 10°, and 20°.

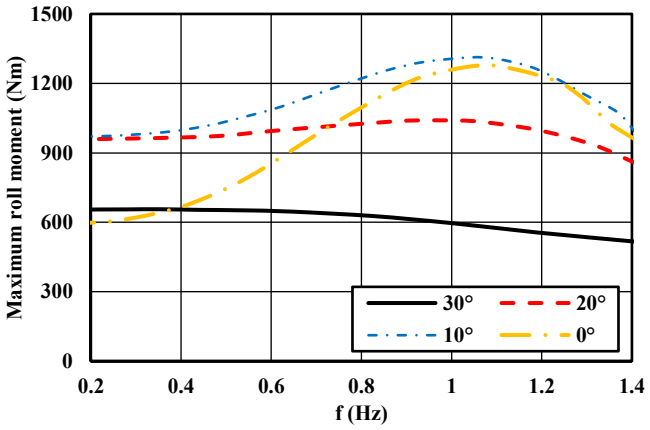

Figure 14. Roll wave moments at different heel angles.

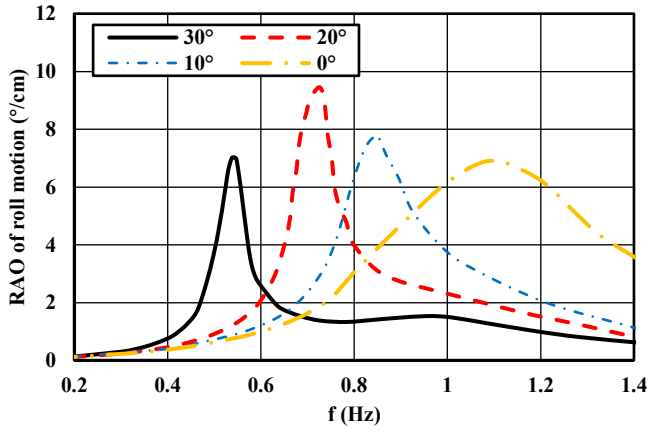

Figure 15. Roll RAO at different heel angle.

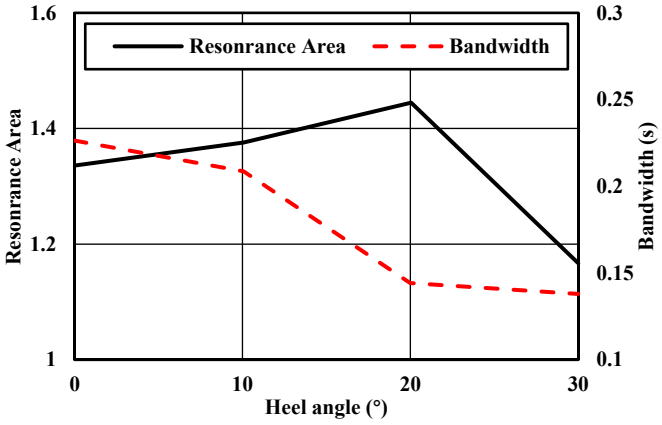

Figure 16. Area and bandwidth at different heel angles.

3.5. Effect of Wave Incident Angles in Frequency Domain

To investigate the influence of wave incident angles on device performance, the floater is positioned at 0°, 10°, 20°, and 30° relative to the incident wave direction. The hub depth and heel angle are set to 0 mm and 0°, respectively. The wave incident angle is defined as the angle between the incident wave direction and the positive X-axis direction.

As shown in Figure 17, the roll wave moment first increases and then decreases with the wave period under different incident angles. Moreover, the roll wave moment decreases significantly as the wave incident angle increases. This indicates that the roll wave moment can be effectively altered by adjusting the angle between the device and the incident wave. Therefore, the wave incident angle can be optimized to enhance the wave force during normal operation and reduce it during storm conditions. This strategy not only improves the device's energy conversion efficiency in operational sea states but also enhances its safety under extreme environmental conditions.

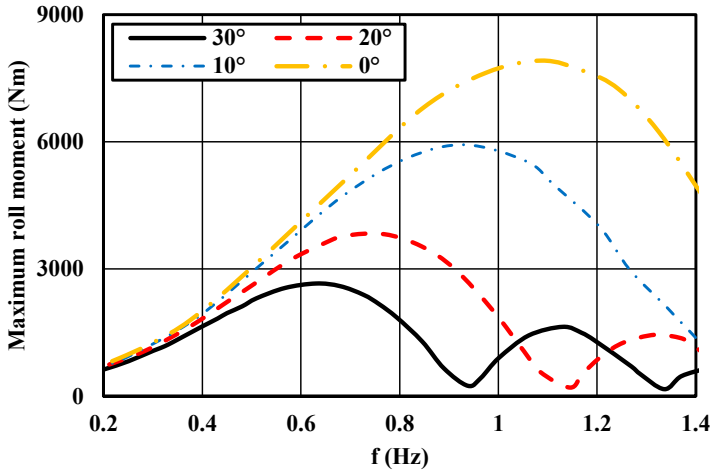

Figure 17. Roll wave moment at different wave incident angles.

Figure 18 demonstrates that the roll RAO decreases significantly as the wave incident angle increases. This is primarily due to the substantial reduction in the roll wave moment with increasing wave incident angle, while the resonance period of the WEC remains relatively unchanged, as the wave has little effect on the wetted surface of the device.

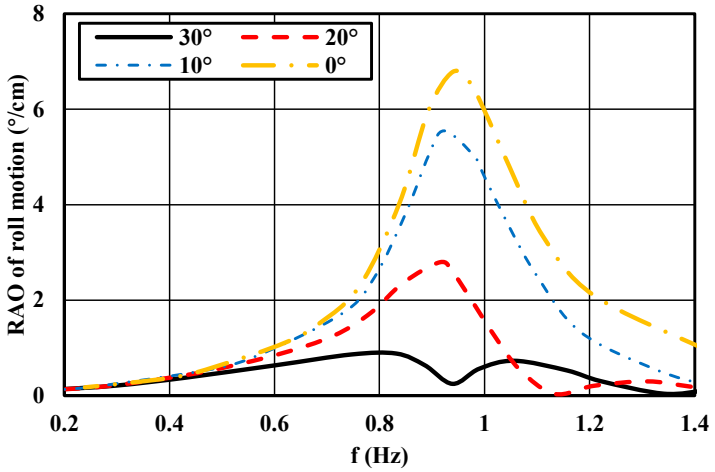

Figure 18. Roll RAO at different wave incident angles.

The area and bandwidth of the region vary with the wave incident angle, as shown in Figure 19. When the wave incidence angle ranges from 0° to 20°, the resonance area

decreases significantly, while the bandwidth remains relatively stable. When the wave incidence angle increases from 20° to 30°, the resonance area increases slightly, and the bandwidth expands considerably. The bandwidth is particularly wide at a wave incident angle of 30°, due to the reduced roll motion response. Therefore, to enhance the efficiency of the device, it is recommended to adjust the device so that the wave incidents vertically.

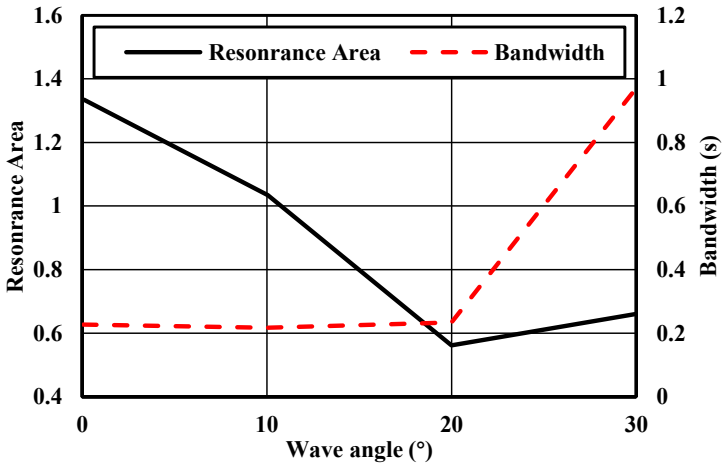

Figure 19. Area and bandwidth under different wave incident angles.

4. Time Domain Results

In the time domain, the coupled dynamic response of the device is analyzed, and the power generation and efficiency are subsequently calculated, providing a valuable reference for the design of roll-type WEC.

4.1. Mooring System

Regarding the mooring mode of the WEC, many researchers tend to favor the multi-point mooring configuration over the single point mooring mode due to the high associated costs. In this study, four mooring cables are employed to constrain the device, with the layout illustrated in Figure 2. A tension mooring method is adopted, and the mooring cables are modeled as linear elements, meaning that their submerged mass is neglected and cable nonlinearities are not considered. Therefore, the mooring cables conform to the static tension relationship.

$$\Delta L = T/k \tag{3}$$

$$F_T = T = k * \Delta L \tag{4}$$

where ΔL is the elongation of the cable, k is the elastic coefficient, T is the cable tension, and F_T is the mooring force.

4.2. Numerical Validation

The tests of the roll-type WEC were conducted in the towing tank at the School of Naval Architecture, Dalian University of Technology. The tank has a length of 160 m, a width of 7 m, and a depth of 3.5 m. A wave maker is installed at the front end, and the rear end is equipped with a wave absorber to minimize interference caused by reflected waves. The device is restrained by four mooring cables. One end of each steel cable is connected to the outer ring of the bearing, while the other end is attached to a tension sensor near the pulley, as illustrated in Figures 20–24.

The mooring system consists of steel cables, pulleys and springs. To make the mooring system similar to a tensioned mooring, a spring is connected in the middle of the steel cable. The role of the pulleys is to change the direction of the mooring line so that the mooring

force can be measured on shore by a tension sensor, which not only reduces the operation difficulty of the test, but also lowers the cost. Mooring pre-tension can be adjusted by changing the initial elongation of the spring. The experimental mooring system comprises four steel cables, each with a diameter of 4 mm and a linear mass density of 18.2 g/m. A buffer spring, characterized by a stiffness coefficient of 400 N/m and a mass of 200 g, is connected in series at the midpoint of each cable. Under static water conditions and in the upright floating state, the initial tension applied to each mooring spring is 28 N. The fairlead of the mooring system is positioned at a height of 0 m, corresponding to the free water surface level when the device is in its upright floating configuration. The underwater pulley is located 1.12 m vertically below the water surface.

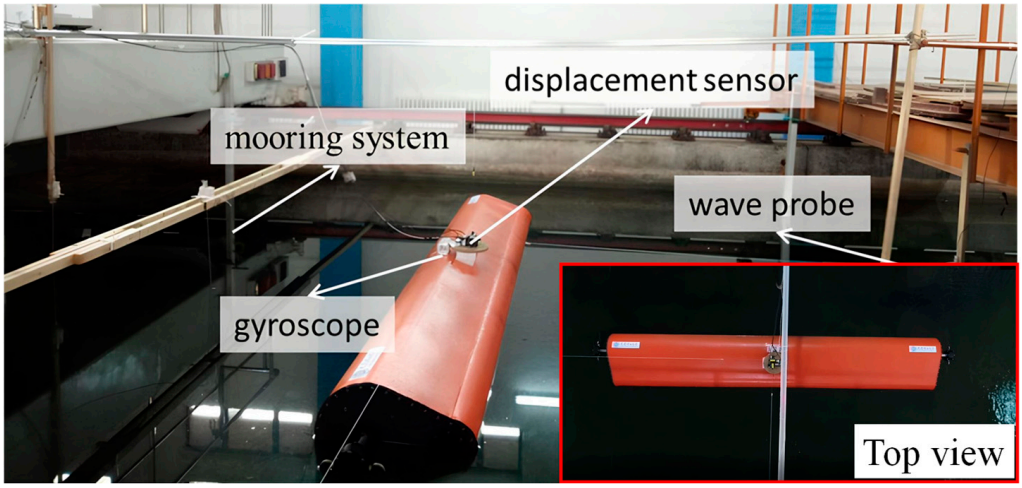

Figure 20. Test equipment.

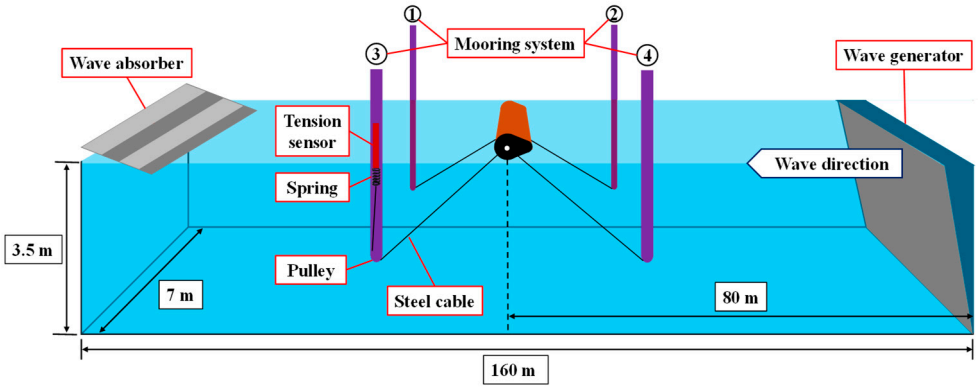

Figure 21. Overview of experimental layout.

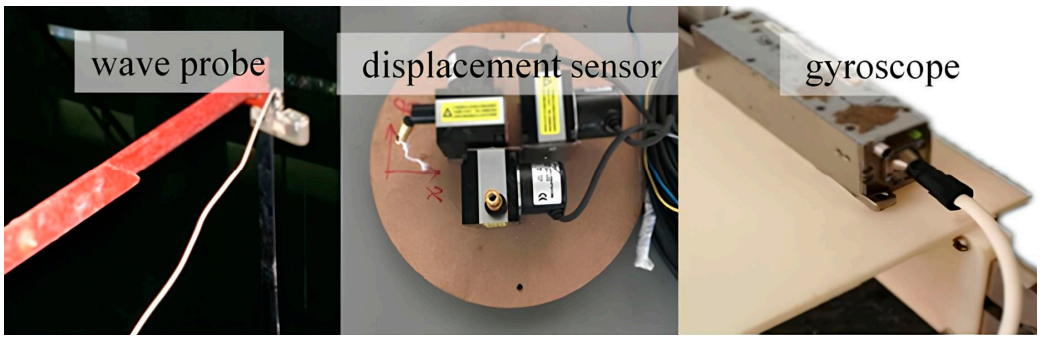

Figure 22. Sensor instrumentation in experiment.

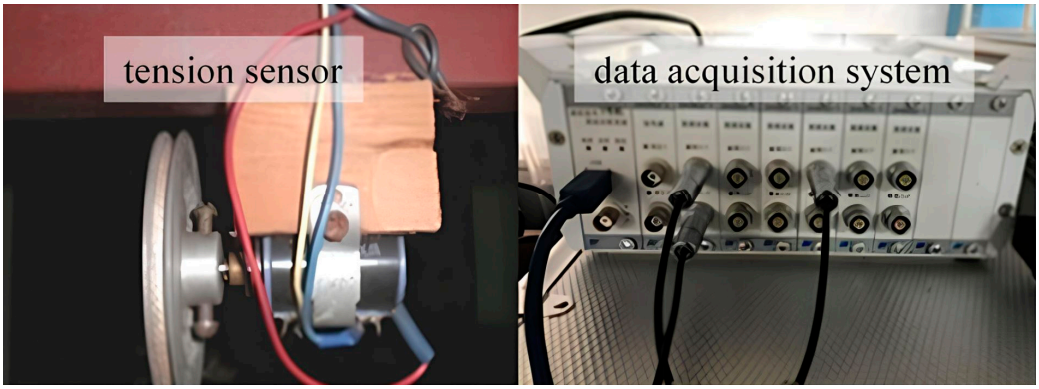

Figure 23. Data acquisition system.

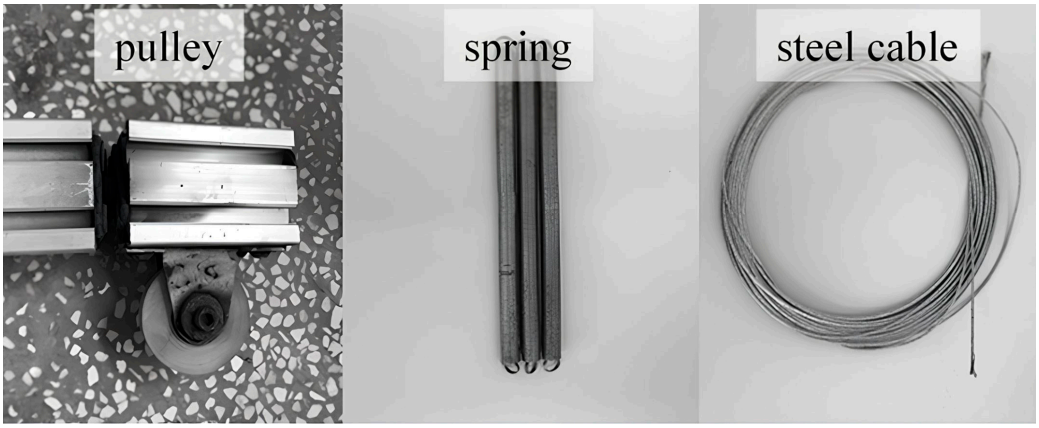

Figure 24. Components of the mooring system.

Wave probes are arranged in a linear configuration on the seaside and leeside of the device to monitor the incident and diffracted wave envelopes. The calibration constant of the wave probes is determined to be 1 m/V. Displacement sensors are employed to measure sway, surge, and heave motions, with a calibration constant of 0.2 m/V. A gyroscope is used to capture roll, pitch, and yaw motions, achieving an accuracy of $\pm 0.1\%$. Tension sensors are mounted on the frame to measure mooring forces, and their calibration constant is also found to be 1 m/V. Sensor signals are collected and processed by the data acquisition system, subsequently transmitted to the computer, and finally displayed, recorded, and stored in real time by the acquisition software.

The scale ratio applied in the experimental setup matches that of the numerical model, with both set at 1:25.

The numerical method employed in this study is based on 3D potential flow theory, which neglects the viscous effects of water. To compensate for this limitation, viscous effects are incorporated in the form of equivalent damping. The equivalent damping coefficient is obtained from the free roll decay test of the model, and the dimensionless equivalent damping value is 0.0259. Figures 25 and 26 present comparisons between the numerical and experimental results for the roll response of the device. It can be observed from the figures that the numerical and experimental results are in good agreement, indicating that the numerical model is reliable for calculating and analyzing the motion behavior of the device.

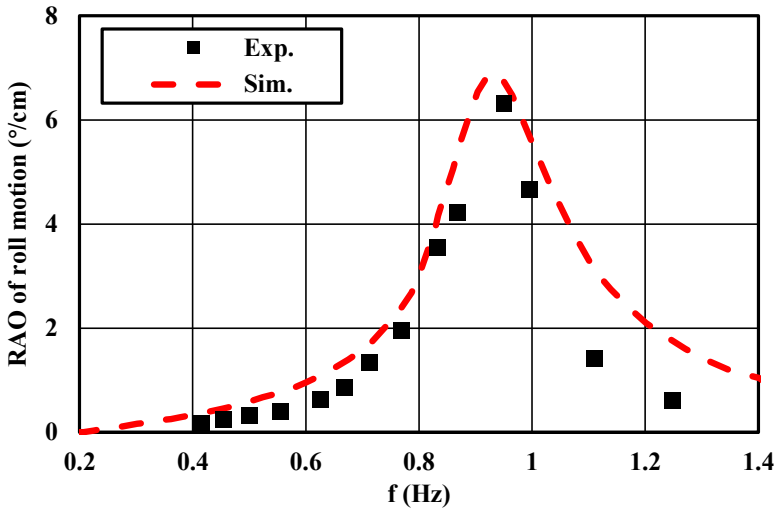

Figure 25. Comparisons of test and numerical roll motion of Roll RAO.

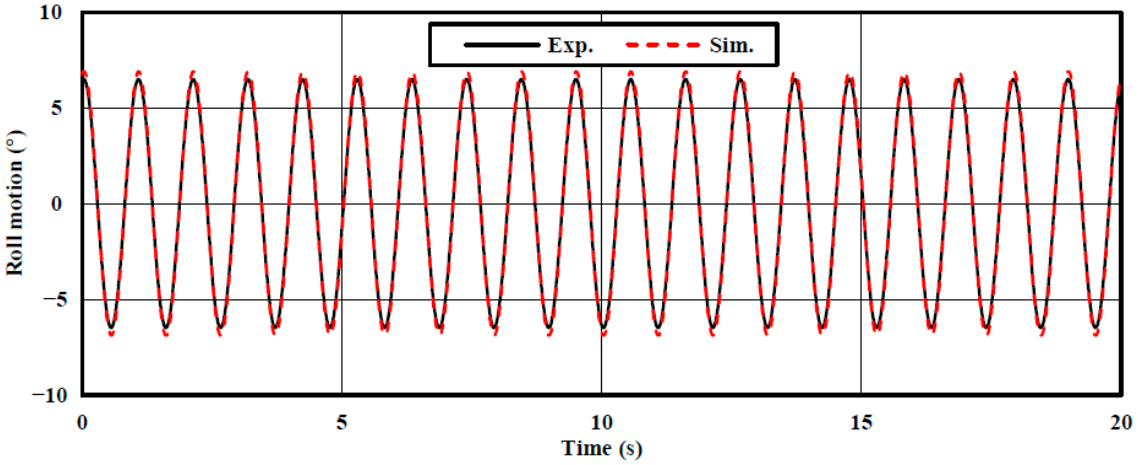

Figure 26. Comparisons of tests and numerical roll motion of Roll.

4.3. Mooring Force in Time Domain

The mooring system in the experiment is shown in Figure 26. The mooring forces of cables No. 1 and No. 3 are equal, and those of cables No. 2 and No. 4 are also equal, due to the symmetrical arrangement of the mooring system on the XOZ plane. The mooring forces of cables No. 2 and No. 4 are greater than those of cables No. 1 and No. 3. This phenomenon can be attributed to the influence of the slow wave drift force, which causes the device to move away from its equilibrium position toward the incoming wave direction. As a result, the mooring forces on the seaside are greater than those on the leeside.

4.4. Power Generation and Efficiency

In this study, the effect of the PTO system on the roll-type WEC is simplified as an equivalent linear damping applied to the device. This equivalent damping can be regarded as the electromagnetic impedance produced by the generator. The work performed by the electromagnetic impedance corresponds to the generated electrical energy. The equivalent damping of the PTO system is applied to the roll motion of the device in the form of damping moment [39]. Damping moment can be expressed as:

$$M_d = \lambda_d \omega \tag{5}$$

where M_d is the damping moment, λ_d is the equivalent linear damping and ω is the roll angular velocity. The average power generation of the device under regular wave in a cycle is:

$$P_{ave} = \frac{1}{T}\int_0^T M_d v dt \tag{6}$$

where P_{ave} is the average power generation and T is the wave period. In monochromatic 3D regular waves, the wave power contained in the wave period per unit width is:

$$P_{wave} = Ec_g \tag{7}$$

where E is the total energy in the next wave period per unit width and c_g is the group velocity of the wave. The Equation (7) represents the energy flux of monochromatic long-crested waves and does not specify the energy distribution among degrees of freedom. The total energy in the next wave period per unit width is:

$$E = \frac{1}{8}\rho g H^2 \tag{8}$$

where ρ is the density of water, g is the acceleration of gravity and H is the wave height. The group velocity of wave in infinite water depth is as follows:

$$c_g = \frac{g}{2\omega} \tag{9}$$

where ω is the wave circle frequency. Therefore, the efficiency of the device under regular waves can be expressed as:

$$\eta = \frac{P_{ave}}{P_{wave}L} \tag{10}$$

where L is the projected length of the device in the direction of the vertically incident wave.

Figure 27 illustrates the influence of equivalent linear PTO damping on the performance of the wave energy converter (WEC) across various wave periods. Figure 27a displays the electrical power output generated by the Power Take-Off (PTO) system. Figure 27b presents the wave absorption efficiency, defined as the ratio of the mechanical power captured by the WEC hull from the incident waves (prior to electromechanical conversion) to the wave-excited power. This efficiency metric is calculated using the excitation moments detailed in Equations (5)–(10) and characterizes the hydrodynamic energy extraction capability of the WEC hull itself, independent of the non-idealities of the PTO's electrical generator.

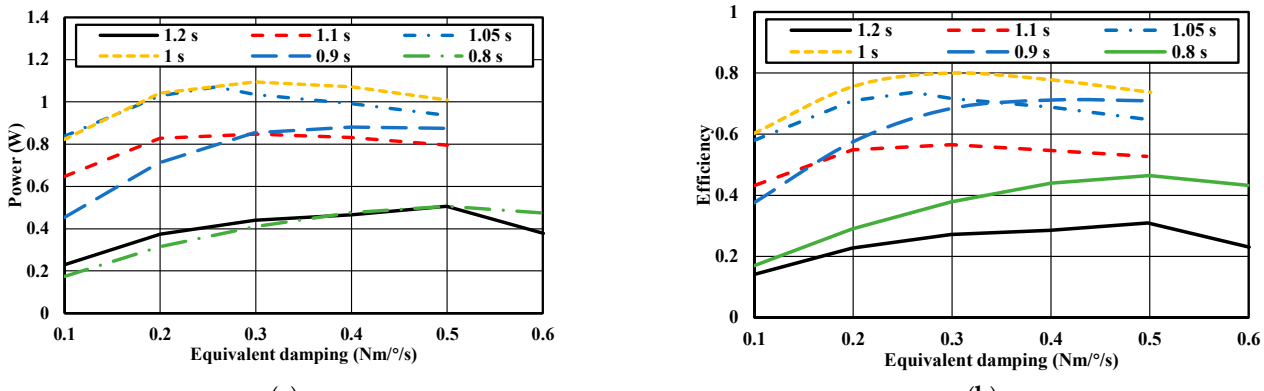

(**a**) (**b**)

Figure 27. Power generation and efficiency vary with equivalent damping at different wave periods: (**a**) Power; (**b**) Efficiency.

Both subfigures indicate that the electrical power output and the absorption efficiency exhibit a non-monotonic dependence on the equivalent linear damping, reaching maximum values at an optimal damping level for each wave period. This confirms the presence of an optimal PTO damping configuration that maximizes either electrical power generation or hydrodynamic energy capture under specific wave conditions. Importantly, the trends observed in electrical power (Figure 27a) and absorption efficiency (Figure 27b) differ, particularly with respect to the location of the optimal damping coefficient. This discrepancy arises because the electrical power output is influenced by the non-ideal and nonlinear characteristics of the electrical generator (e.g., energy losses and saturation effects), whereas the absorption efficiency primarily reflects the hydrodynamic interaction between the WEC and the waves.

Furthermore, the results show that peak performance—both in terms of electrical power and absorption efficiency—is achieved when the wave period matches the roll resonance period of the device. For wave periods shorter than the roll resonance period, the optimal equivalent linear damping coefficient decreases with increasing wave period. Conversely, for wave periods longer than the roll resonance period, the optimal equivalent linear damping coefficient increases as the wave period increases.

It is noteworthy that the capture efficiency demonstrates remarkably high values for a system with a single degree of freedom. This behavior can be explained by the resonance effect that arises when the roll frequency closely matches the wave frequency, resulting in a significant enhancement of energy absorption efficiency—particularly under regular wave conditions. Under such conditions, the resonance of roll motion leads to a continuous buildup of energy until a steady state is reached, which may result in a measured roll amplitude that exceeds that observed in irregular waves encountered in real sea states.

Power and efficiency initially increase and subsequently decrease with increasing wave period, as shown in Figure 28. The wave period corresponding to the peak value is 1 s, which is close to the resonance period. The optimal equivalent linear damping first decreases and then increases with the wave period, reaching its minimum at 1.05 consistent with the roll resonance period. This indicates that the optimal equivalent linear damping is minimized during resonance. Within the resonance region, both the maximum power generation and efficiency are high, with only minor variations. These values are concentrated between 0.85 W and 1.15 W, and between 57% and 80%, respectively.

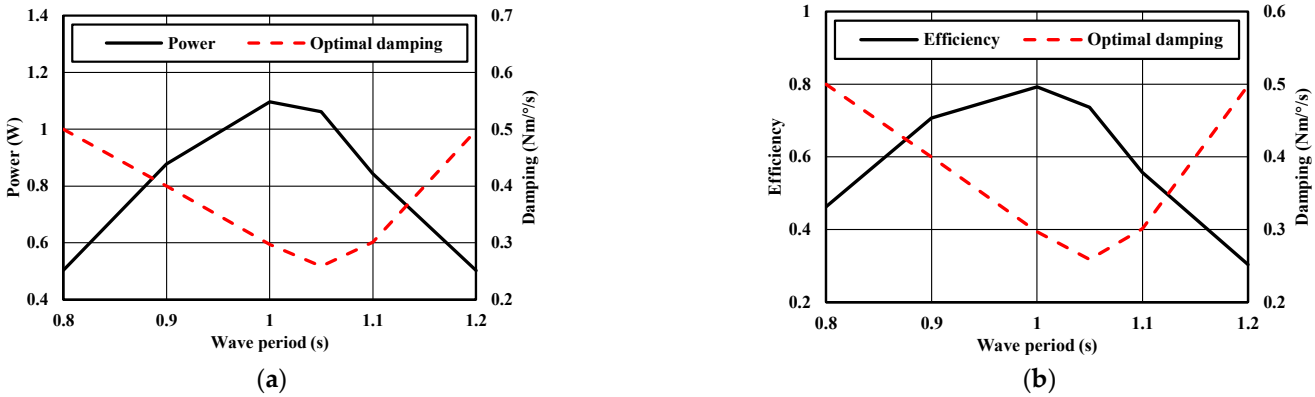

Figure 28. Maximum generation and efficiency and optimal equivalent damping: (**a**) Power; (**b**) Efficiency.

4.5. Effect of Axial Depth in Time Domain

According to the results presented in Section 3.4, both the power generation and power efficiency of the device are high within the resonance region. Therefore, the wave period used for the calculations corresponds to the roll resonance period, and the wave height is set to 0.02 m. As shown in Figure 29, both the generated power and the generation efficiency

first increase and then decrease with increasing equivalent damping. This indicates that, for each axial depth, there exists an optimal equivalent linear damping that maximizes power and efficiency. The highest power generation and efficiency are achieved at an axial depth of 20 mm. When the axial depth ranges from 0 to 40 mm, both power generation and efficiency remain high with minimal variation. However, between 40 and 60 mm axial depth, power generation and efficiency are significantly reduced due to a substantial decrease in the roll wave moment.

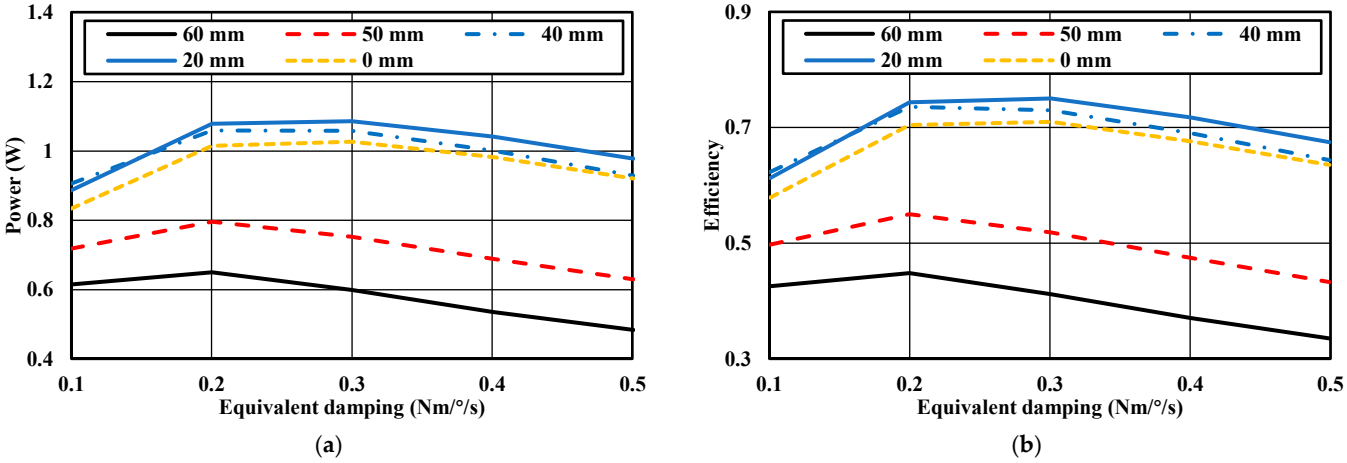

Figure 29. Power generation and efficiency at different axial depths: (**a**) Power; (**b**) Efficiency.

Figure 30 shows that both power generation and efficiency initially increase gradually with axial depth and subsequently decrease. The maximum values of power generation (1.087 W) and efficiency (75%) are achieved at an axial depth of 20 mm. This is consistent with the results obtained from the qualitative analysis of device efficiency based on the resonance region and bandwidth in the frequency domain, thereby verifying the reliability of the analytical method.

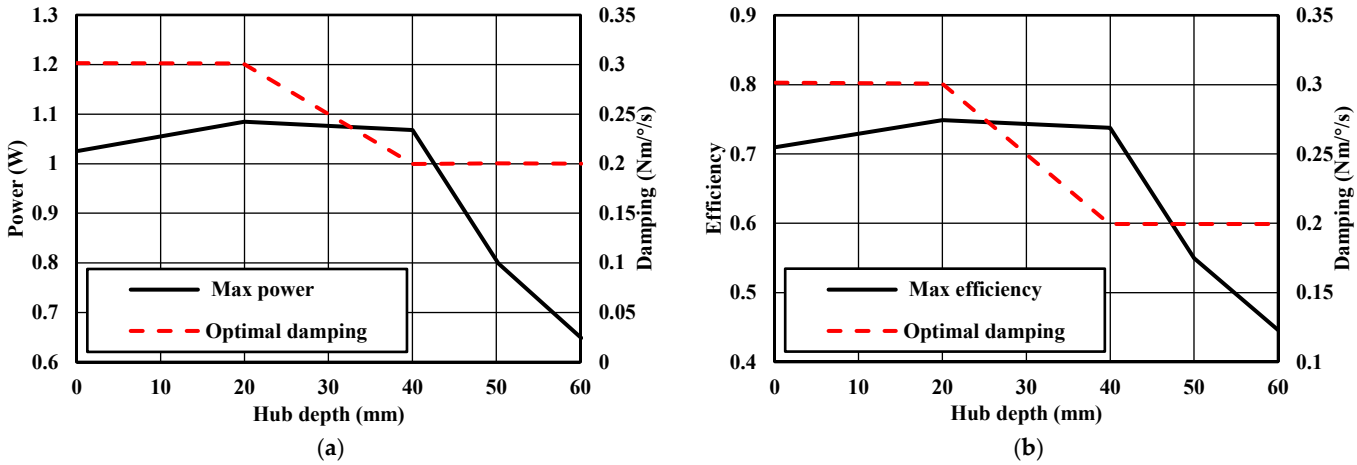

Figure 30. Maximum generation and efficiency and optimal damping at different hub depth: (**a**) Power; (**b**) Efficiency.

4.6. Effect of Heel Angle in Time Domain

The wave condition used for calculation is selected following the same methodology as described in the previous section. Figure 31 illustrates that both power generation and efficiency initially increase and subsequently decrease with the increase in equivalent damping. This indicates that, for each heel angle, there exists an optimal equivalent linear damping value that maximizes power generation and efficiency. When the PTO

system damping is considered, the maximum power generation and efficiency occur at a 0° heel angle. In contrast, when the PTO system is not considered, the floater's efficiency in converting wave energy into roll mechanical energy peaks at a 20° heel angle. The observed phenomenon can be attributed to the narrow bandwidth of the resonance region at 20° heel angle. A narrower bandwidth implies a greater sensitivity to damping, which leads to reduced power generation and efficiency when PTO system damping is present. Therefore, PTO damping should be considered in the design of WECs. At larger heel angles, the resonance period increases, and the resonance region becomes narrower, resulting in a decline in both power generation and efficiency.

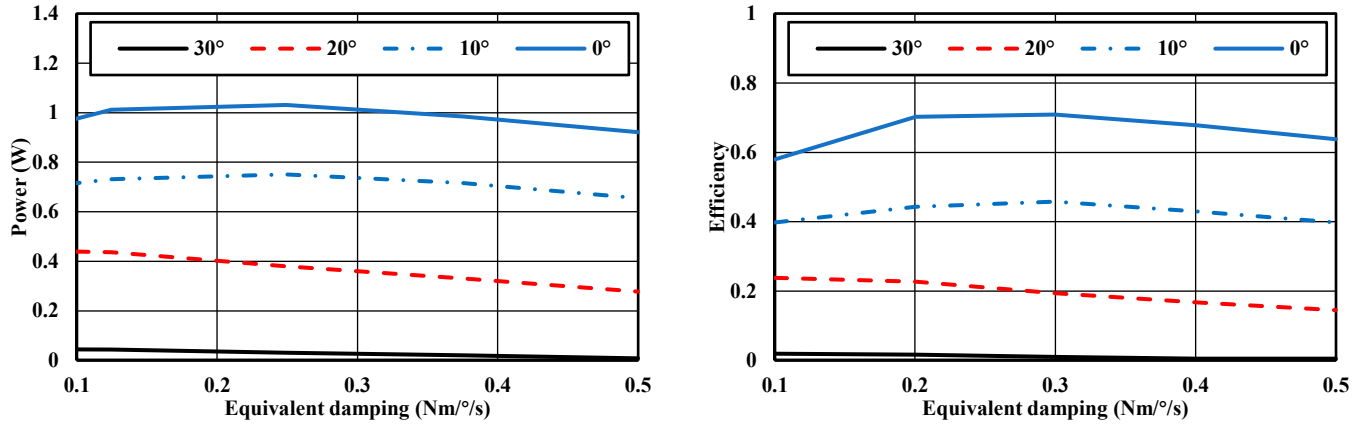

Figure 31. Power generation and efficiency at different heel angles: (**a**) Power; (**b**) Efficiency.

Figure 32 shows that both power generation and efficiency decrease with increasing heel angle, indicating that an increase in heel angle does not contribute to improving power generation or efficiency. The maximum values of power generation and efficiency, 1.03 W and 71%, are achieved at a 0° heel angle.

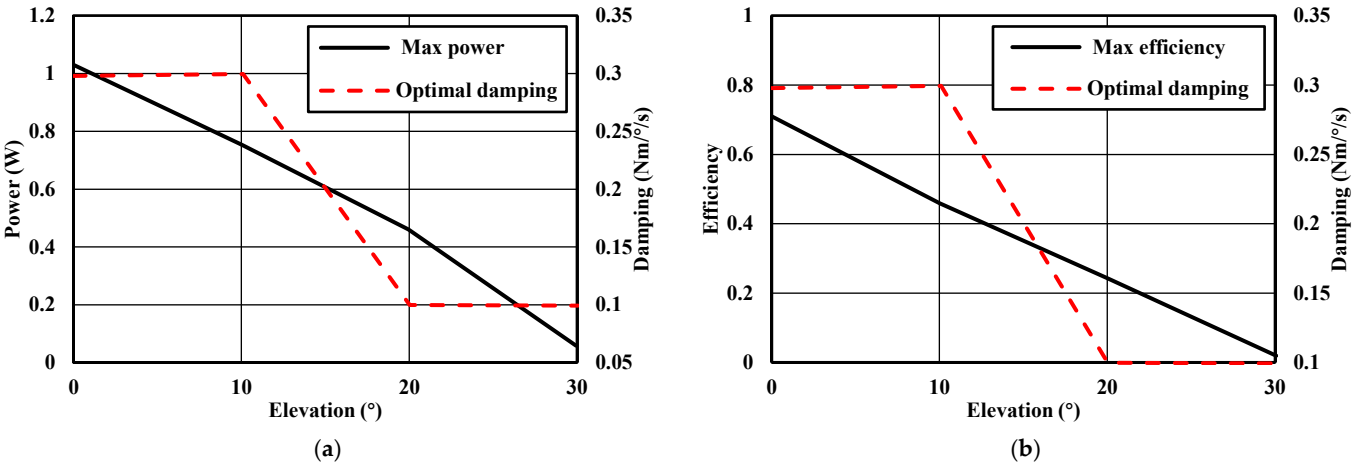

Figure 32. Maximum generation and efficiency and optimal damping at different heel angle: (**a**) Power; (**b**) Efficiency.

4.7. Effect of Wave Incident Angle in Time Domain

According to the results presented in Section 4.4, the device achieves maximum power generation and efficiency when the equivalent PTO linear damping is set to 0.26 Nm/deg/s and the wave period corresponds to the resonance period. The wave incident angle is an external condition that does not influence the intrinsic properties of the device, indicating that the optimal equivalent damping remains unaffected by the direction of the incident

wave. Therefore, in the simulation, the wave period is set to the roll resonance period, the equivalent PTO linear damping is 0.26 Nm/deg/s, and the wave height is 0.02 m. Figure 33 shows that both power generation and efficiency decrease significantly with increasing wave incident angle. The highest values, 1.03 W for power generation and 71% for efficiency, are observed at a 0° wave incident angle. When the wave incident angle exceeds 20°, the efficiency drops below 10%. Thus, to ensure optimal power generation and efficiency, the device should be arranged to receive waves perpendicularly.

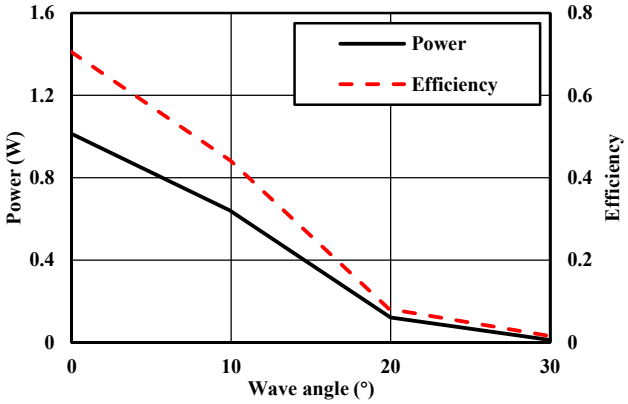

Figure 33. Maximum generation power and efficiency at different wave angles.

4.8. Performance of the Device Under Irregular Waves

The performance of the device under regular waves has been analyzed in previous sections. However, the actual operating conditions of wave energy converters (WECs) occur in real marine environments, which are more accurately represented by irregular wave conditions. In the simulation, the JONSWAP spectrum was selected as the target spectrum. The wave spectrum peak period was set to the roll resonance period, the significant wave height was 0.02 m, the equivalent PTO linear damping was 0.26 Nm/deg/s, the axis depth was 0 mm, the heel angle was 0°, and the wave incident angle was also 0°.

The sway, heave, and roll motions under irregular waves are presented in Figures 34–36. The maximum values of sway, heave, and roll motion are 0.088 m, −0.028 m, and 4.664°, respectively, while the minimum values are 0.065 m, −0.044 m, and −3.182°, respectively. The mean values are 0.077 m, −0.036 m, and 0.715°, with corresponding standard deviations of 0.004 m, 0.002 m, and 1.220°. It can be observed that the heave motion is relatively small, whereas the roll motion is significantly larger. This indicates that the majority of the wave energy absorbed by the device is converted into roll mechanical energy, further demonstrating the effectiveness of the device design. The non-zero meaning values of sway, heave, and roll suggest the presence of steady-state offsets. Specifically, the sway offset is induced by wave drift forces, while the offsets in heave and roll result from the pretension in the mooring lines. Figures 37–39 show the sway, heave, and roll wave forces under irregular wave conditions. The maximum wave forces for yaw, heave, and roll are 123.056 N, 156.728 N, and 19.990 Nm, respectively, while the minimum values are −129.769 N, −151.294 N, and −20.771 Nm, respectively. The mean values are 0.322 N, −0.040 N, and −0.0001 N, with standard deviations of 37.434 N, 46.678 N, and 6.134 Nm, respectively.

The maximum mooring forces of mooring lines No. 1 and No. 2 are 32.064 N and 31.025 N, respectively, while the minimum values are 24.164 N and 25.109 N, respectively. The mean values are 28.093 N and 28.224 N, with standard deviations of 1.308 N and 1.055 N, respectively. As shown in Figures 40 and 41, the mooring force on the seaside is greater than that on the leeside. The temporal variation pattern of the mooring force is strongly correlated with the heave motion, despite differences in their physical dimensions and magnitudes. This indicates that the variation in mooring force is primarily induced by heave motion.

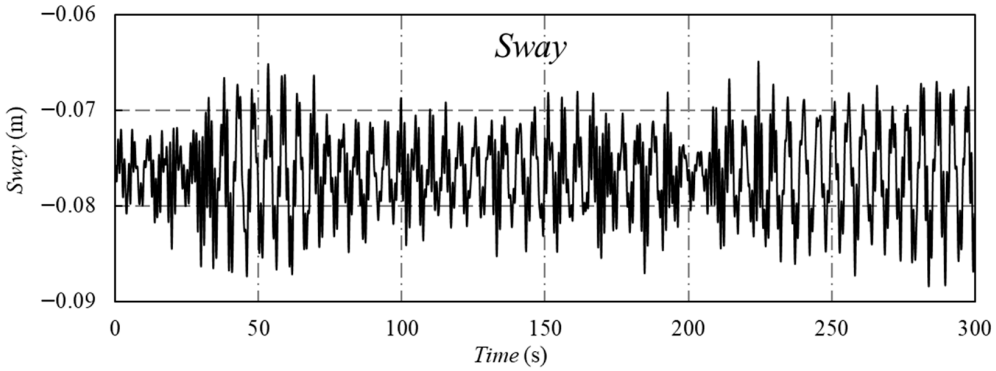

Figure 34. Sway motion of WEC under irregular waves.

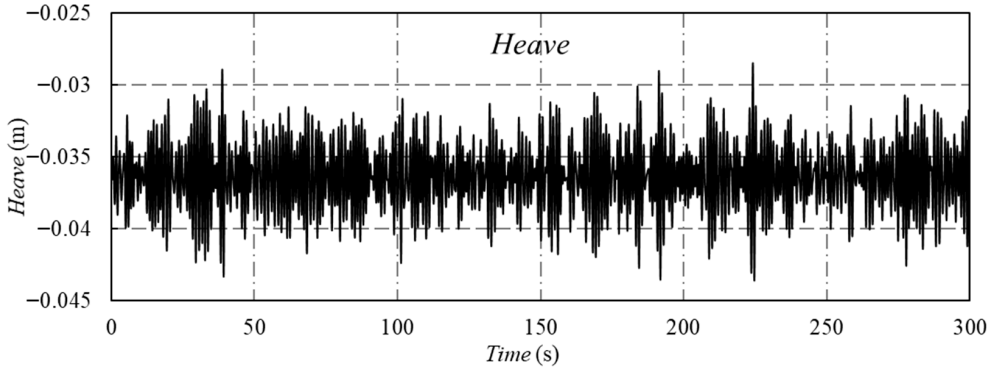

Figure 35. Heave motion of WEC under irregular waves.

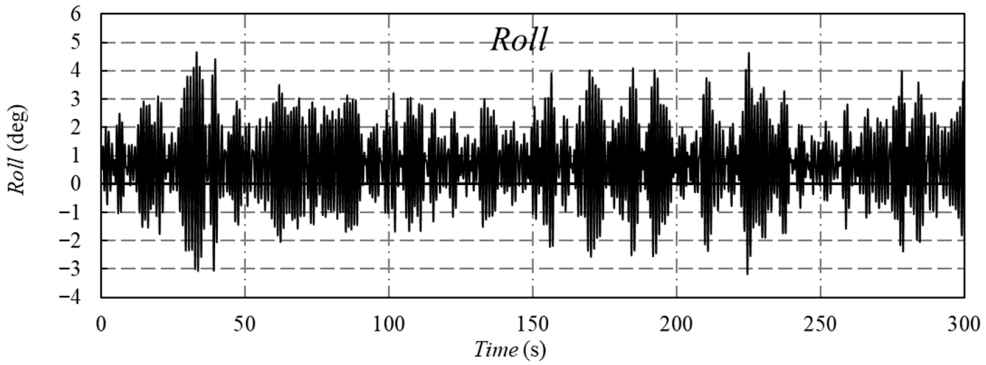

Figure 36. Roll motion of WEC under irregular waves.

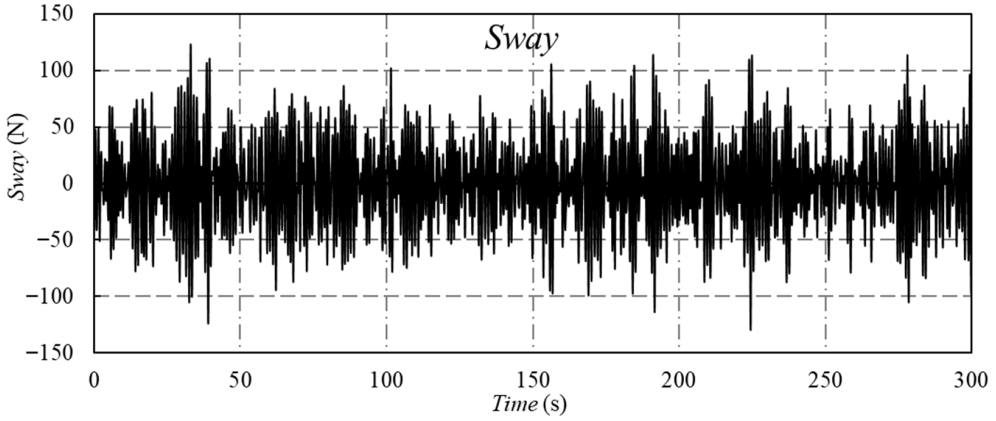

Figure 37. The force of sway motion under irregular waves s.

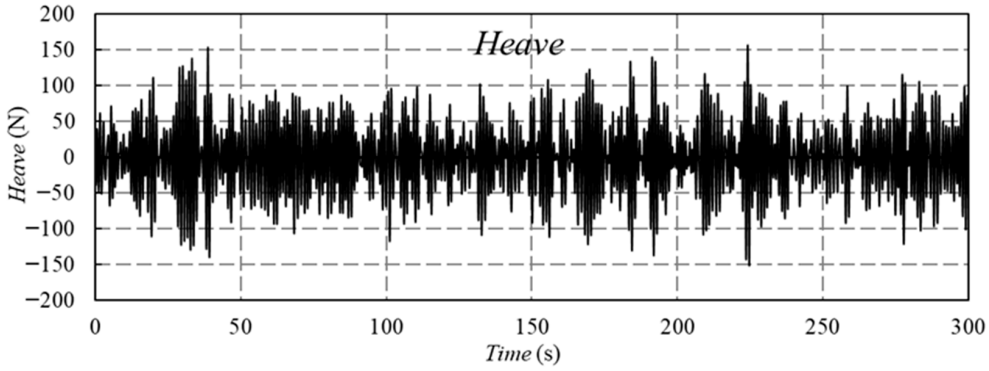

Figure 38. The force of heave motion under irregular waves.

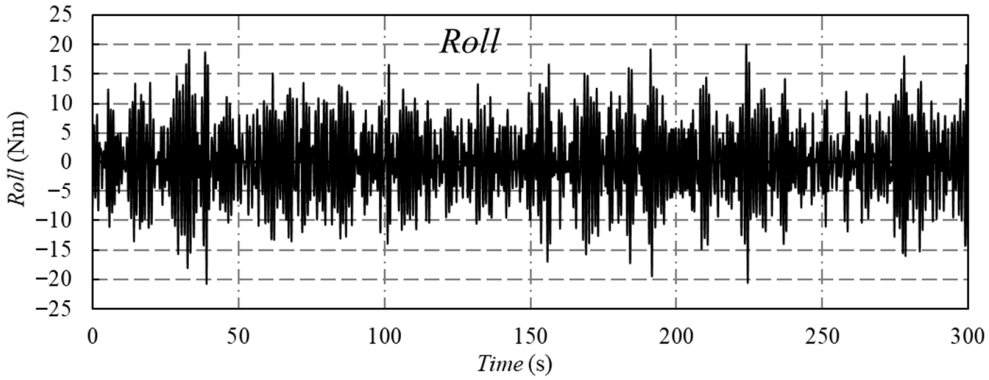

Figure 39. The moment of roll motion under irregular waves.

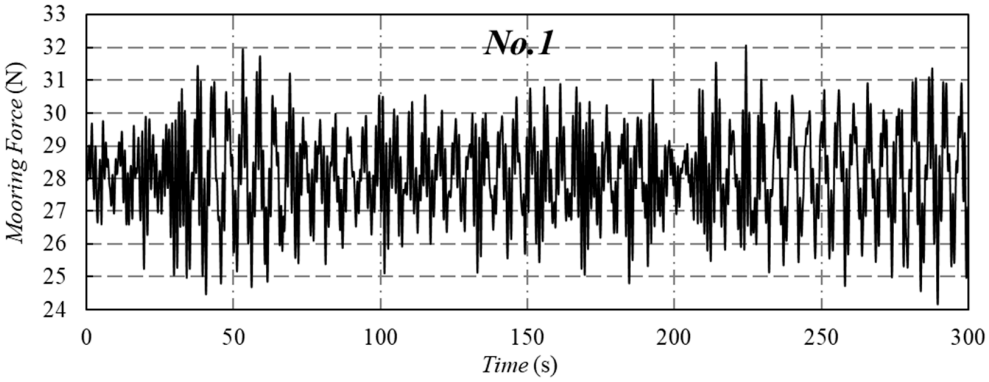

Figure 40. Typical mooring force of No. 1.

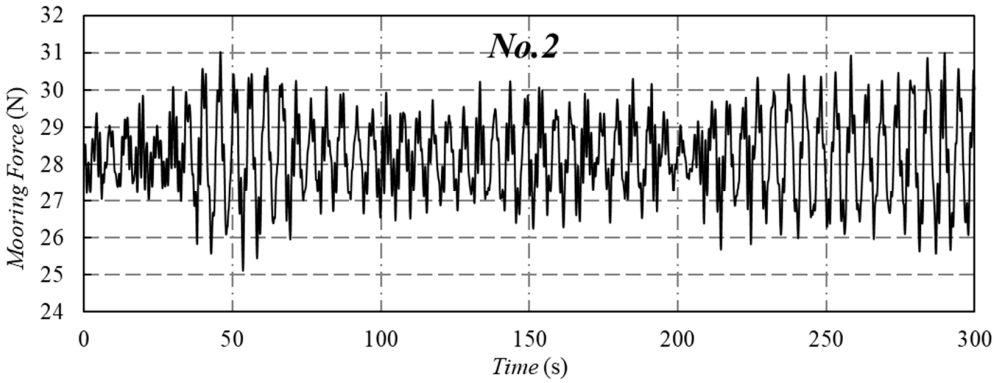

Figure 41. Typical mooring force of No. 2.

Under irregular waves, the average power is as follows:

$$\overline{P} = \frac{1}{t_1 - t_0} \int_{t_0}^{t_1} \lambda_d v^2 dt \tag{11}$$

where $\overline{P}$ is the average power of the device in the period from t_0 to t_1. Under irregular waves, the available wave power and efficiency can be expressed as:

$$P_{ir} = \rho g \int_0^{\infty} S(\omega) C_g d\omega \tag{12}$$

$$\eta_{ir} = \frac{\overline{P}}{P_{ir} L} \tag{13}$$

where $S(\omega)$ is the power spectral density. When the spectral peak period of the irregular wave is 1.05 s and the significant wave height is 0.02 m, the power generating and efficiency within 300 s are 0.248 w and 38%, respectively.

Power generation and efficiency initially increase and subsequently decrease with the increase of the spectral peak period, as illustrated in Figure 42. When the spectral peak period approaches the roll natural period, both power generation and efficiency reach higher values, a trend consistent with the behavior observed under regular wave conditions. The maximum power generation and efficiency are 0.248 W and 39%, respectively.

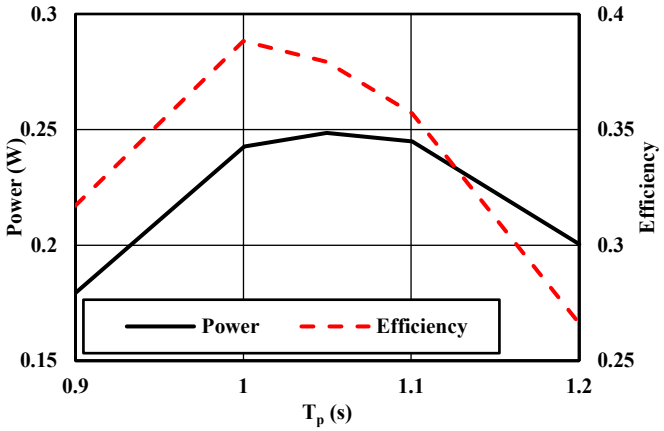

Figure 42. Generation power and efficiency.

Figure 43 demonstrates that both power generation and efficiency decline rapidly as the wave incident angle increases. When the wave is incident perpendicular to the device, the maximum power and efficiency are achieved, a pattern consistent with that observed under regular wave conditions. When the wave incident angle exceeds 20°, the efficiency drops below 5%. Therefore, during operation, it is recommended that the device be aligned as perpendicularly as possible to the incident waves in order to optimize efficiency.

As shown in the figure above, after multiple rounds of optimization, the WEC device investigated in this study can convert nearly 40% of incident wave energy into mechanical energy under irregular wave conditions. To facilitate a comparative assessment of the wave energy absorption efficiency of this WEC device, Figure 44 presents a comparison of the maximum efficiencies reported in the literature for various WECs with different characteristic widths under full scale conditions [40].

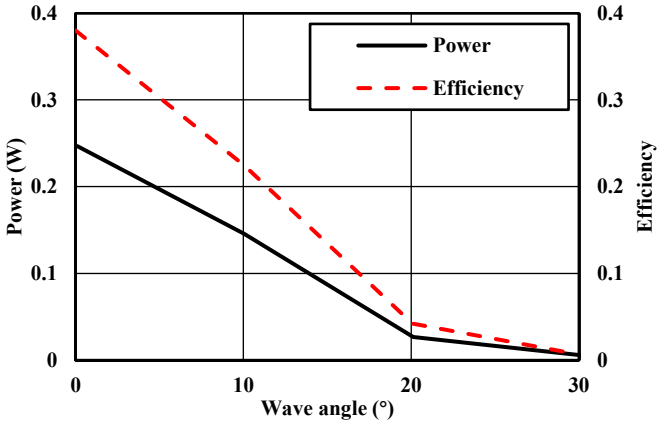

Figure 43. Generation power and efficiency at different wave incident angles.

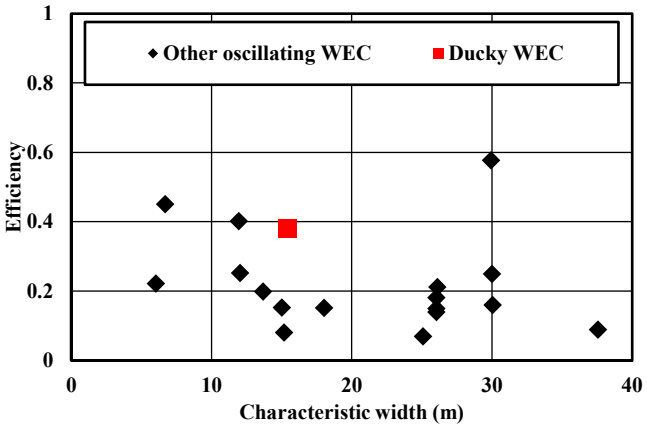

Figure 44. Power generation efficiency of oscillating WEC under full scale.

Numerous studies in the literature have reported on the power performance of various WECs. In this study, only those WECs that were evaluated under irregular wave conditions, either through experimental testing or numerical simulation, were selected when compiling the efficiencies of different WECs. The efficiencies reported in this paper primarily focus on the maximum power captured by the WECs. Given that WECs are typically designed to achieve optimal performance under specific irregular wave conditions, the efficiencies presented here generally reflect the best achievable performance of each device, even though the conditions in which they were tested or simulated varied in terms of wave characteristics and occurrence probabilities [40].

The improved device proposed in this study has demonstrated notable advantages in comparative industry efficiency assessments, with energy capture performance surpassing the industry average and placing it in the upper-middle range. Although the current efficiency has not yet reached the theoretical or laboratory-determined maximum, significant breakthroughs have been achieved in engineering practicality and system integration. The device is securely anchored to the seabed via a robust mooring system, ensuring positional stability under varying sea states and forming a solid foundation for efficient energy conversion. Its key innovation lies in the fully enclosed design, wherein critical components are hermetically sealed to withstand the corrosive effects of the marine environment, thereby achieving exceptional reliability and durability. This design significantly reduces maintenance demands and lifecycle costs, making the device particularly well-suited for long-term deployment in deep-sea and offshore environments. A distinctive feature of the device is its strategic deployment in the peripheral zones of floating offshore wind farms, where it not only captures wave energy for power generation but also serves as an effective wave attenuator. By reducing the wave energy that reaches the turbine

platforms, it functions as a dynamic "buffer zone" for the wind farm. This synergistic effect markedly stabilizes the pitch, roll, and heave motions of the wind turbine foundations, thereby improving both the energy output efficiency and structural safety of the wind turbines, and enabling complementary enhancement of wave and wind energy utilization. Looking forward, continued efforts will be directed toward optimizing the device's design, further investigating the underlying mechanisms of energy capture and conversion, and striving to overcome existing efficiency limitations. These improvements aim to enhance the overall performance and economic viability of the system, contributing more robust solutions for the efficient, stable, and large-scale deployment of marine renewable energy.

5. Influence of the Wave Energy Converter on Floating Wind Turbine

Both offshore wind and wave energy are abundant marine energy resources with substantial development potential. However, the utilization of single energy sources faces challenges such as high development costs and low operational stability. As a result, multi-energy complementarity has emerged as a promising and viable solution. Integrated wave-wind energy systems offer several technical advantages, including reduced power variability, increased energy output within a given project area, cost reductions through shared electrical grid connections and foundation substructures, and improved operational and maintenance logistics. Among these benefits, the wave attenuation effect provided by the WEC plays a critical role in reducing the motion response of floating offshore wind turbines under combined wind and wave loading conditions. To quantify this effect, the difference in wave height before and after the WEC is analyzed. This section examines the co-location of an offshore wind turbine and a WEC, with a focus on the pitch motion response of the NREL 5 MW baseline wind turbine mounted on the OC4-DeepCwind semi-submersible platform, which is positioned downstream of the roll WEC. The simulation presented in this section is based on a full-scale model.

5.1. Parameters of the Marine Wave Environment

Linear wave superposition method is used to simulate the selected irregular wave. Ocean waves evolution can be thought of as a stationary random process, which can be comprised of M ($M \to \infty$) cosine waves with different periods and different random initial phases. Therefore, we may represent the vertical displacement as the sum of numerous frequency components:

$$\eta(x,t) = \sum_{i=1}^{M} a_i cos(k_i x - \omega_i t + \varepsilon_i) \tag{14}$$

where, η is the instantaneous height of the fluctuating free surface relative to the stationary water surface, x and t represent position and time. For component i, a_i is the wave amplitude, k is the wave number ($k_i = 2\pi/L_i$), ω_i is the circular frequency ($\omega_i = 2\pi/T_i$), L_i and T_i are wave length and period, respectively, and ε_i is a random initial phase, ranging from 0 to 2π.

Usually, the interest is limited to nearly uni-directional sea waves, and they are simulated through the JONSWAP spectrum. As shown in Figure 45, the energy of the target spectrum $S(\omega)$ to be simulated is mostly distributed between $\omega_L \sim \omega_H$ and the rest can be ignored. Generally, it is sufficient to take 3~4 times the frequency of spectral peak as ω_H. The equal frequency interval can be expressed as $\Delta\omega = (\omega_H - \omega_L)/M$. When the position is fixed, $x = 0$ is desirable. Under the circumstances, the equation can be simplified as follows:

$$\eta(x=0,t) = \sum_{i=1}^{M} \sqrt{2S(\omega)\Delta\omega} cos(-\omega_i t + \varepsilon_i) \tag{15}$$

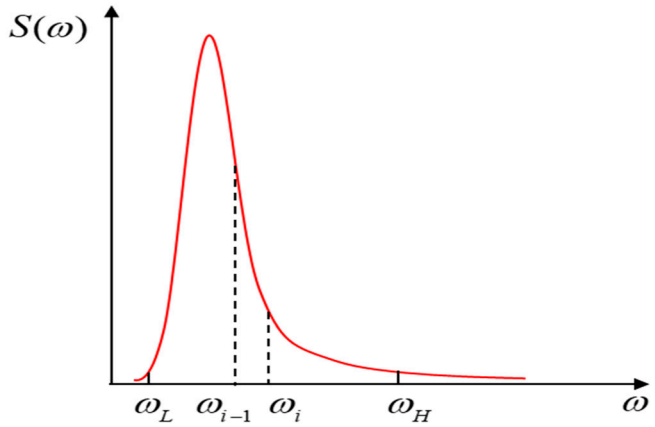

Figure 45. Schematic diagram of target spectrum division.

As for the environmental conditions, an irregular wave with a significant wave height of 3.9 m and a peak period of 7.78 s is selected to investigate the difference between the incident wave and the attenuated wave behind the WEC. Based on the JONSWAP spectrum and the linear wave superposition method, unidirectional irregular waves with a significant wave height of 3.9 m and a peak period of 7.78 s are simulated. The specified irregular wave is evenly divided into 100 cosine wave components within the frequency range of 0.56 rad/s to 1.56 rad/s, with an equal frequency interval $\Delta\omega$ = 0.01 rad/s. The simulated wave height before and after the wave generator is presented in Figure 46. It is evident that the wave height after the wave generator is significantly reduced compared to that before the generator, indicating that the wave generator possesses considerable wave attenuation capability.

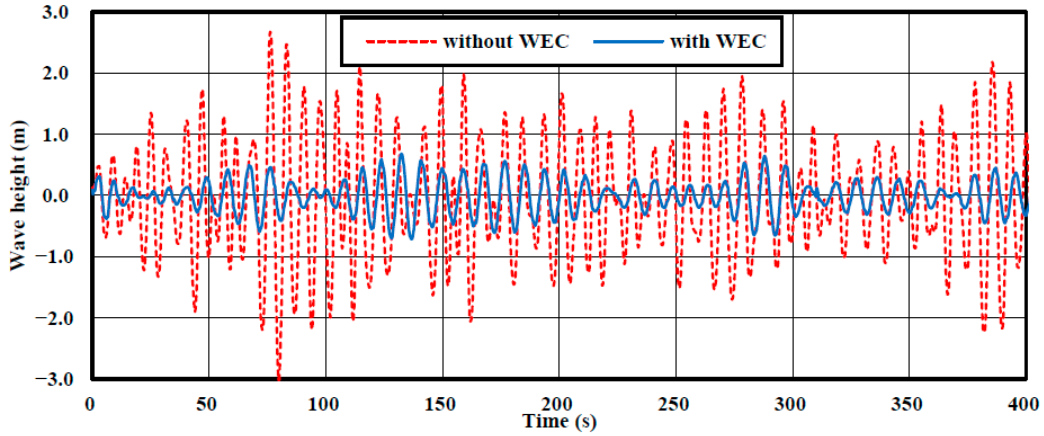

Figure 46. The comparison of wave height before and after the wave energy converter.

The wave parameters were measured at two locations: at the WEC, 100 m upstream along the wave propagation direction, representing the undisturbed upstream waves, and 100 m downstream, corresponding to the waves after they had passed through the WEC. The waves at these two measurement points are denoted as "without WEC" and "with WEC" in the figure, respectively. Additionally, the planned installation site of the FOWT in the future is also set at a distance of 100 m from the WEC.

To investigate the relationship between wave height variation in the frequency domain and the motion response of the FOWT, and to assess the wave energy absorption and filtering performance of the WEC, the power spectral density (PSD) of the wave height-time

series data was computed. This study adopts the Welch method to calculate the PSD [41]. The specific process is as follows:

$$PSD(f_k) = \frac{1}{K}\sum_{i=1}^{K}\frac{1}{F_s U}|FFT(x_i\omega)|^2$$
$$U = \frac{1}{L}\sum\omega^2[m] \quad (16)$$

The signal, sampled at a rate of F_s, is segmented into K overlapping segments, each with a length of L, which corresponds to 50% of the total data length. However, L is constrained to be no less than the minimum number of points required to achieve a frequency resolution of 0.001 Hz. A 50% overlap is maintained between consecutive segments. To minimize spectral leakage, each segment is multiplied by Hann Window before computing the modified periodogram. The periodograms from all K segments are then averaged to obtain the final PSD estimate.

The resulting one-sided PSD is reported within the frequency range of 0.001–0.5 Hz as shown in Figure 47.

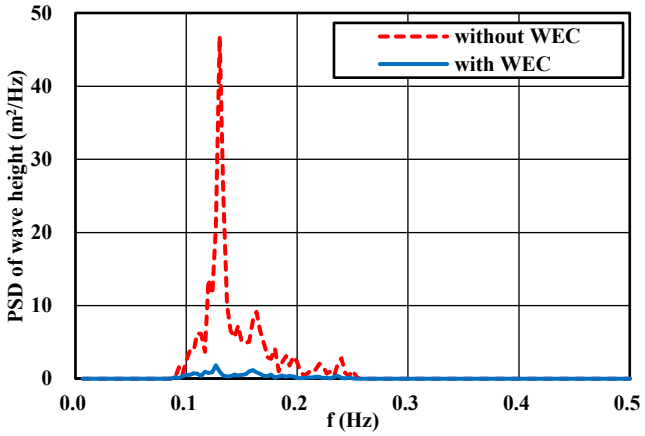

Figure 47. PSD of wave height before and after the wave energy converter.

It is evident that the wave height experiences a notable decline both upstream and downstream of the WEC. Significantly, most of the wave energy fails to propagate to a location 100 m beyond the WEC. By performing statistical analysis on the wave information presented in Figure 37, the resulting wave parameters are summarized in Table 3.

Table 3. Parameters of the irregular waves.

Parameters	Without WEC	With WEC
Tp (s)	7.783	7.788
Hs (m)	3.882	1.173

5.2. Simulational Model and Case Setup

In most offshore wind farms, WECs are installed upstream of floating wind turbines. This arrangement can mitigate the hydrodynamic effects of waves on floating platforms to a certain extent without reducing wind speed, thereby maximizing the utilization of marine energy. In this section, during the integration of the offshore wind turbine and WEC, the WEC is positioned 100 m upstream of the downstream wind turbine, as shown in Figure 46. The wave power device employs the roll wave energy generation technology described in Section 2, while the NREL 5MW baseline wind turbine mounted on the OC4-DeepCwind semi-submersible platform is selected as the floating offshore wind turbine.

The main paraments of the OC4-DeepCwind semi-submersible platform are listed in Table 4. Numerical simulations of the floating offshore wind turbine (FOWT) were conducted using OpenFAST v8 through a computational approach. For the selection of input waves, two sets of wave data were considered: one representing wave passing through the WEC and the other representing waves without interacting with the WEC, as shown in Figure 37. These wave conditions were used as incident wave inputs to analyze and compare the changes in the motion response of the FOWT before and after the installation of the WEC. A mean velocity of 8 m/s was applied as the superimposed wind condition. Subsequently, full-scale fully coupled numerical simulations were implemented using the validated OpenFAST framework. These simulations based on the integrated "5MW_OC4Semi_WSt_WavesWN" demonstration case within OpenFAST's computational architecture, ensuring consistency with industry-standard semi-submersible platform configurations. The total duration of the physical simulation is 3600 s, with a time step size of 0.01 s.

Table 4. Parameters of the phase II of OC4 FOWT system.

Parameters	Value
Number of blades	3
Rotor, hub diameter (m)	126, 3
Hub height (m)	90
Rotor mass-1 (kg)	110,000
Nacelle mass-2 (kg)	240,000
Tower mass-3 (kg)	347,460
Coordinate Location of CM-1,2,3 (m)	(−0.2, 0, 64.0)
Total draft of platform (m)	20
Volume of displacement (m^3)	13,917
Platform mass (kg)	1.3473×10^7
Coordinate location of CM of platform (m)	(0, 0, −13.46)
Number of mooring lines	3
Angle between adjacent lines (°)	120
Depth to anchors/fairleads below SWL (m)	200, 14
Radius to anchors/fairleads (m)	837.6, 40.868
Unstretched mooring line length (m)	835.5
Mooring line diameter (m)	0.0766
Equivalent extensional stiffness (N/m)	7.536×10^8
Equivalent mass density/in water (kg/m)	113.35, 108.63
Total mass of the FOWT system (kg)	1.417×10^7
Global CM location below SWL (m)	9.6475
Total structure roll inertia about CM ($kg \cdot m^2$)	1.1×10^{10}
Total structure pitch inertia about CM ($kg \cdot m^2$)	1.1×10^{10}
Total structure yaw inertia about CM ($kg \cdot m^2$)	1.226×10^{10}

To simplify the calculations and minimize the impact of other factors, the blades of the wind turbine generator and the tower cylinder are assumed to be unreformable rigid bodies.

5.3. Comparison of Motion Response of FOWT Before and After the Wave Energy Converter

As illustrated in Figures 48 and 49, the pitch and heave motions of the FOWT are compared before and after the installation of the WEC device. To ensure data stability, the data segment ranging from 3000 to 3600 s was selected for comparison and visualization. The simulation visualization is presented as depicted in Figure 50.

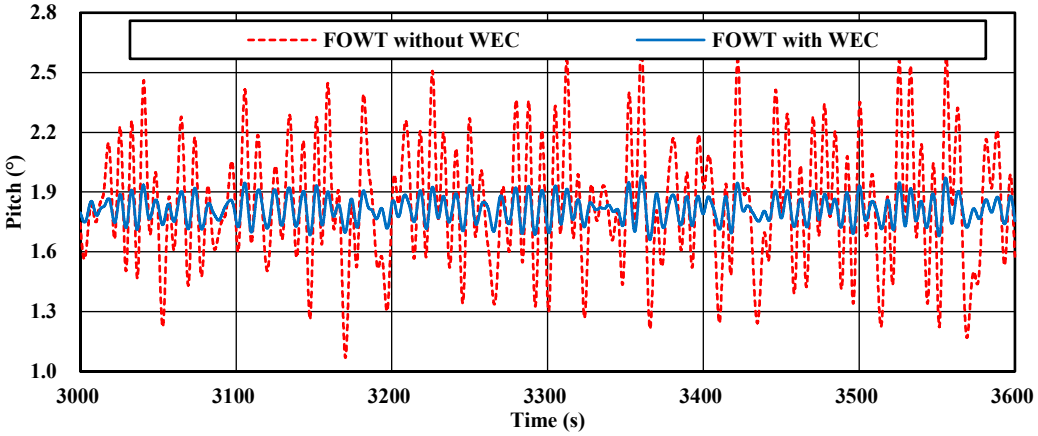

Figure 48. The comparison of pitch motion responses.

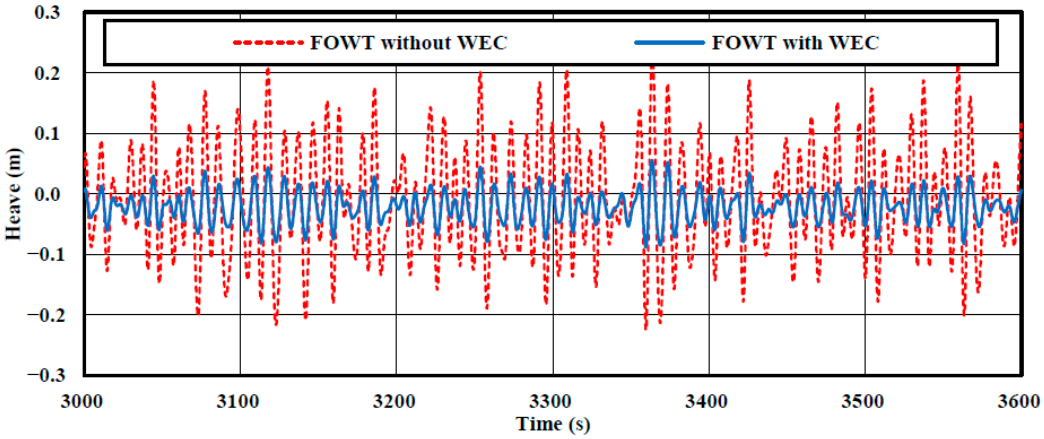

Figure 49. The comparison of heave motion responses.

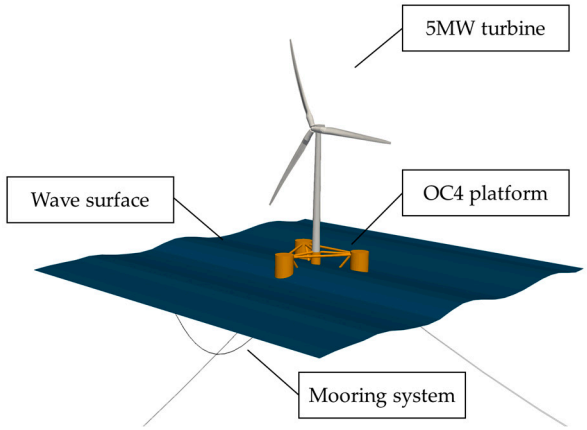

Figure 50. Simulation visualization.

In this figure, the 'FOWT without WEC' data corresponds to the motion response of the FOWT only, occurring when waves directly interact with the FOWT without WEC influence, whereas the 'FOWT with WEC' data reflects the FOWT's motion response behind WEC, where waves pass through the WEC before interacting with the FOWT.

To quantitatively evaluate the degree of stabilization imparted to the floating platform by incorporating the WEC, the time-domain data for pitch and heave were processed to extract the significant values of motion amplitudes, as presented in Table 5.

Table 5. The significant values of motion amplitudes.

Parameters	FOWT Without WEC	FOWT with WEC	Relative Error
Pitch (°)	0.8959	0.2165	−75.834%
Heave (m)	0.3291	0.0965	−70.678%

In terms of the differences, the performance parameters of FOWT, such as power generation and power generation stability, exhibit significantly higher sensitivity to the pitch motion of the floating platform compared to other motions. Through a comparison of the pitch motion results, it is evident that the integration of the WEC results in a significant reduction in the amplitude of the pitch motion of the FOWT. The heave motion response of the FOWT positioned downstream of the WEC is significantly smaller compared to that of the upstream FOWT. This is attributed to the fact that the pitch and heave motion response is directly correlated with the wave height of the selected irregular wave. Furthermore, under head sea wave conditions, the differences in motion across other degrees of freedom are relatively insignificant.

To quantitatively assess the energy distribution across different frequency bands and to identify dominant response frequencies as well as potential resonant peaks, we have performed PSD analysis on the time history signals of pitch and heave under all investigated irregular sea conditions. The results are presented in Figures 51 and 52.

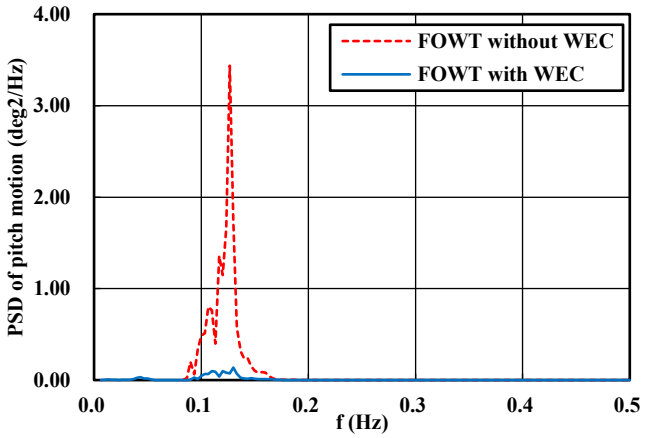

Figure 51. PSD of pitch motion.

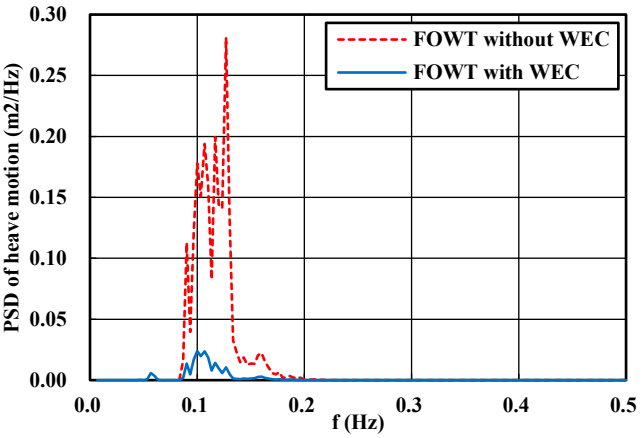

Figure 52. PSD of heave motion.

From the frequency domain perspective, prior to the integration of the WEC, the energy distribution of the platform's motion exhibited a relatively consistent pattern with

that of the irregular waves. However, upon incorporating the WEC, a substantial reduction in motion energy was observed for both the heave and pitch of the platform. This suggests that the WEC effectively mitigates the influence of wave energy on the platform, thereby enhancing its motion stability.

Additionally, to systematically analyze the influence of integrating WEC on load variations at critical locations of FOWT and to quantify the degree of deviation from the mean value, the data were subjected to dimensionless processing. For stability comparison, the data in the table are represented by the ratio of the significant value of motion amplitude to its mean value. A larger dimensionless number indicates greater motion instability. The formula for dimensionless number of the variable change amplitude is as follows:

$$D = \frac{A_{1/3}}{\overline{A}} \tag{17}$$

where, D represents the dimensionless number of the variable change amplitude; $A_{1/3}$ represents the significant value of the variable change amplitude; $\overline{A}$ represents the average value of the variable change. The results are presented in Table 6 below.

Table 6. Dimensionless loads of FOWT.

Parameters	FOWT Without WEC	FOWT with WEC	Relative Error
Rotor azimuth angular speed	0.023	0.004	−82.625%
Nacelle fore-aft translation	0.997	0.275	−72.388%
Tower base fore-aft shear force	0.874	0.157	−81.991%
Tower base axial force	−0.009	−0.002	−79.224%
Tower base pitch moment	0.970	0.228	−76.540%
Power generation	0.098	0.020	−79.773%

It is evident from the table that the addition of WEC significantly enhances the stability of the overall load on the wind turbine. Wave-induced material fatigue across of the wind turbine is mitigated substantially. The wind turbine's power variation is presented in Figure 53.

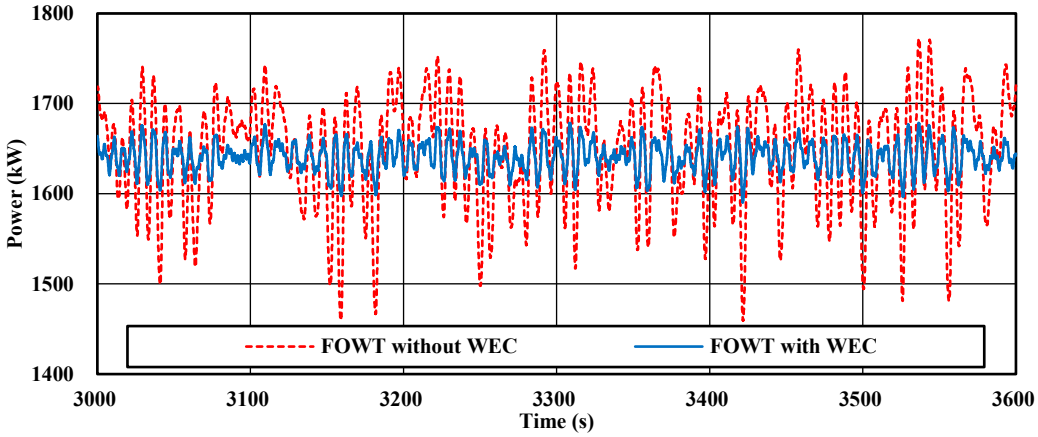

Figure 53. Power generation of the wind turbine.

When comparing FOWT with WEC to FOWT without WEC, the average power output of FOWT with WEC decreased by 0.46%. This slight reduction can likely be attributed to the reduced pitch motion. Nonetheless, FOWT with WEC significantly enhanced the stability of power generation, leading to reduced control system losses, decreased overall maintenance frequency, and ultimately lower maintenance costs.

Consequently, deploying ducky-WECs around the wind farm can markedly improve the stability of power generation, extend the expected service life of the wind turbine, and optimize other operational parameters. This approach offers numerous advantages, including reduced engineering costs and enhanced overall economic benefits for the project.

6. Conclusions

To enhance the performance evaluation of the device, a numerical model of the roll wave energy converter (WEC) incorporating both the mooring and power take-off (PTO) systems was developed. Wave forces and response amplitude operators (RAOs) were calculated in the frequency domain, and a qualitative method for assessing conversion efficiency based on the area and bandwidth of the resonance region was proposed.

Frequency domain analysis reveals that when the shaft depth is 20 mm, both the roll resonance region area and bandwidth reach their maximum values, resulting in the highest wave energy conversion efficiency. When the side tilt angle is 20°, the roll resonance region area is maximized, leading to the highest efficiency in converting wave energy into roll mechanical energy. As the wave incidence angle increases, the resonance region area rapidly diminishes, with normal wave incidence yielding the highest conversion efficiency. The time-domain simulation of the system without the power take-off (PTO) under regular wave conditions showed good agreement with experimental results, confirming the reliability of the established numerical model. The influence of the PTO system on power generation and efficiency under various sea states was investigated. Results indicate that for any given sea condition, there exists an optimal damping value that maximizes both power output and efficiency. When the wave period is shorter than the resonance period, the optimal damping decreases as the wave period increases; conversely, it increases when the wave period exceeds the resonance period. At resonance, the optimal damping reaches its minimum value. As the wave period approaches the resonance period, resonance occurs, causing the motion response, power generation, and efficiency to attain their peak values. When the shaft depth is set at 20 mm, the device achieves its maximum power generation capacity and efficiency (1.087 W, 75%). The highest power generation and efficiency are observed at a side tilt angle of 0° and a wave incidence angle of 0°, which aligns well with the qualitative findings from the frequency domain analysis. Under irregular wave conditions, the device exhibits significant roll motion, while heave and sway motions remain relatively small. The force variation in mooring line No. 2, on the wave-facing side, is greater than that in mooring line No. 1, on the wave-sheltered side. When the peak wave period approaches the roll resonance period, the device demonstrates relatively high-power generation capacity and efficiency, with the maximum efficiency reaching up to 39%. Under random wave conditions, both power generation and efficiency decline rapidly with increasing wave incidence angle, consistent with observations made under regular wave conditions.

Finally, a comparison of wave heights before and after the wave maker revealed a significant reduction in wave height downstream, indicating the device's notable wave attenuation capability. By comparing the motion responses of the OC4-DeepCwind semi-submersible platform wind turbine with and without the WEC, it was demonstrated that the wave attenuation effect of the WEC significantly reduces heave and pitch motion responses. According to the operational conditions investigated in this study, integrating WEC devices can reduce the pitch and heave responses of floating offshore wind turbines (FOWTs) under wave action by over 70%. Furthermore, this integration significantly improves the stability of the generator's output energy, while maintaining the average power generation at nearly the same level. Deploying this device around offshore wind farms can substantially enhance power generation stability, extend the operational lifespan

of wind turbines, optimize operational parameters, reduce engineering costs, and improve the overall economic viability of the project.

Author Contributions: Conceptualization, T.T. and Y.D.; Data curation, T.T., Y.D. and X.G.; Formal analysis, Y.D. and Y.J.; Funding acquisition, Y.J.; Investigation, X.G.; Methodology, Y.D. and X.G.; Project administration, T.T. and X.G.; Resources, Y.J. and Z.Y.; Software, S.L., Y.J. and Z.Y.; Supervision, T.T.; Validation, T.T., Y.D. and S.L.; Visualization, Y.D.; Writing—original draft, Y.J.; Writing—review & editing, Z.Y. All authors have read and agreed to the published version of the manuscript.

Funding: This work was supported by Shenzhen 2022 Key Project for Technological Research [grant number JSGG20220831110803006]; Key Project for Industrial Technological Innovation in Liaoning Province: "Jie Bang Gua Shuai" Project, Research and·Design of 40 Knots High Speed Passenger Cargo Ship.

Data Availability Statement: The data presented in this study are available on request from the corresponding author.

Conflicts of Interest: Tao Tao, Xinran Guo and Shi Liu were employed by the company China Southern Power Grid Technology Co., Ltd. Shi Liu was also employed by the company National Institute of Guangdong Advanced Energy Storage Co., Ltd. The remaining authors declare that the research was conducted in the absence of any commercial or financial relationships that could be construed as a potential conflict of interest.

Abbreviations

The following abbreviations are used in this manuscript:

WEC	wave energy converter
PTO	power take-off
RAO	response amplitude operators
CFD	Computational Fluid Dynamics
EFD	Experimental Fluid Dynamics
FOWT	floating offshore wind turbines
OWC	oscillating water column
OWT	offshore wind turbines
TWWC	TLP-WT-WEC- Combination
OES	Ocean Energy Systems
IRENA	International Renewable Energy Agency
TWh	terawatt-hours
CAGR	Compound Annual Growth Rate

References

1. Jia, J. Investigation in a Ocean Wave Energy Converter with a Flywheel. Master's Thesis, The Graduate School, Stony Brook University, Stony Brook, NY, USA, 2016.
2. Wilberforce, T.; El Hassan, Z.; Durrant, A.; Thompson, J.; Soudan, B.; Olabi, A.G. Overview of ocean power technology. *Energy* **2019**, *175*, 165–181. [CrossRef]
3. Awotwe, T.W.; Alaswad, A.; Mooney, J.; Olabi, A. Hydrogen production for solar energy storage. A proposed design investigation. *State Art Energy Dev.* **2015**, *11*, 353.
4. López, I.; Andreu, J.; Ceballos, S.; De Alegría, I.M.; Kortabarria, I. Review of wave energy technologies and the necessary power-equipment. *Renew. Sustain. Energy Rev.* **2013**, *27*, 413–434. [CrossRef]
5. Anyanwu, R.C.; Rodriguez, C.; Durrant, A.; Olabi, A.G. Optimisation of tray drier microalgae dewatering techniques using response surface methodology. *Energies* **2018**, *11*, 2327. [CrossRef]
6. Rodriguez, C.; Alaswad, A.; Benyounis, K.; Olabi, A.G. Pretreatment techniques used in biogas production from grass. *Renew. Sustain. Energy Rev.* **2017**, *68*, 1193–1204. [CrossRef]
7. Ravindranath, N.H.; Hall, D.O. *Biomass, Energy, and Environment: A Developing Country Perspective from India*; Oxford University Press: Oxford, UK, 1995.

8. Villate, J. Situacion actual de las energías marinas y perspectivas de futuro. In Proceedings of the Seminario Anual de Automatica, Electronica e Instrumentacion, Bilbao, Spain, 7–9 July 2010; pp. 11–13.
9. Deng, Y.-B.; Xiong, W. Development and utilization of ocean energy. *Renew. Energy* **2004**, *3*, 70–72.
10. Fang, Z.F.; Ma, Z.H.; Fang, J.; Gao, S.; He, K.D. Research and development of multi section floating mechanical wave energy power generation device. *Appl. Mech. Mater.* **2014**, *494–495*, 711–716. [CrossRef]
11. Clément, A.; McCullen, P.; Falcão, A.; Fiorentino, A.; Gardner, F.; Hammarlund, K.; Lemonis, G.; Lewis, T.; Nielsen, K.; Petroncini, S.; et al. Wave energy in Europe: Current status and perspectives. *Renew. Sustain. Energy Rev.* **2002**, *6*, 405–431. [CrossRef]
12. Drew, B.; Plummer, A.R.; Sahinkaya, M.N. A review of wave energy converter technology. *Proc. Inst. Mech. Eng. Part A J. Power Energy* **2016**, *223*, 887–902. [CrossRef]
13. Mork, G.; Barstow, S.; Kabuth, A.; Pontes, M.T. Assessing the global wave energy potential. In Proceedings of the International Conference on Offshore Mechanics and Arctic Engineering, Shanghai, China, 6–11 June 2010; pp. 447–454.
14. Gunn, K.; Stock-Williams, C. Quantifying the global wave power resource. *Renew. Energy* **2012**, *44*, 296–304. [CrossRef]
15. Magagna, D.; Uihlein, A. Ocean energy development in Europe: Current status and future perspectives. *Int. J. Mar. Energy* **2015**, *11*, 84–104. [CrossRef]
16. IRENA. *Innovation Outlook: Ocean Energy Technologies*; International Renewable Energy Agency: Abu Dhabi, United Arab Emirates, 2020.
17. Guo, B.; Ringwood, J.V. A review of wave energy technology from a research and commercial perspective. *IET Renew. Power Gener.* **2021**, *15*, 3065–3090. [CrossRef]
18. Khan, N.; Kalair, A.; Abas, N.; Haider, A. Review of ocean tidal, wave and thermal energy technologies. *Renew. Sustain. Energy Rev.* **2017**, *72*, 590–604. [CrossRef]
19. Michailides, C. Hydrodynamic response and produced power of a combined structure consisting of a spar and heaving type wave energy converters. *Energies* **2021**, *14*, 225. [CrossRef]
20. Gaspar, J.F.; Kamarlouei, M.; Thiebaut, F.; Guedes Soares, C. Compensation of a hybrid platform dynamics using wave energy converters in different sea state conditions. *Renew. Energy* **2021**, *177*, 871–883. [CrossRef]
21. Ren, N.; Ma, Z.; Shan, B.; Ning, D.; Ou, J. Experimental and numerical study of dynamic responses of a new combined TLP type floating wind turbine and a wave energy converter under operational conditions. *Renew. Energy* **2020**, *151*, 966–974. [CrossRef]
22. Zhou, Y.; Ning, D.; Shi, W.; Johanning, L.; Liang, D. Hydrodynamic investigation on an OWC wave energy converter integrated into an offshore wind turbine monopile. *Coast. Eng.* **2020**, *162*, 103731. [CrossRef]
23. Falcão, A.F.d.O. Wave energy utilization: A review of the technologies. *Renew. Sustain. Energy Rev.* **2010**, *14*, 899–918. [CrossRef]
24. Pelc, R.; Fujita, R.M. Renewable energy from the ocean. *Mar. Policy* **2002**, *26*, 471–479. [CrossRef]
25. Gomes, M.d.N.; Salvador, H.; Magno, F.; Rodrigues, A.A.; dos Santos, E.D.; Isoldi, L.A.; Rocha, L.A.O. Constructal design applied to geometric shapes analysis of wave energy converters. *Defect Diffus. Forum* **2021**, *407*, 147–160. [CrossRef]
26. Salter, S.H. Wave power. *Nature* **1974**, *249*, 720–724. [CrossRef]
27. Salter, S.H.; Jeffrey, D.C.; Taylor, J.R.M. *First Year Interim Report on Edinburgh Wave Power Project: Study of Mechanisms for Extracting Power from Sea Waves*; University of Edinburgh: Edinburgh, UK, 1975.
28. Jeffrey, D.; Richmond, D.J.; Salter, S.H.; Taylor, J.R.M. *Second Year Interim Report on Edinburgh Wave Power Project 'Study of Mechanisms for Extracting Power from Sea Waves'*; University of Edinburgh: Edinburgh, UK, 1976.
29. Bellamy, N. Wave power experiments at Loch Ness. In Proceedings of the International Conference on Future Energy Concepts, London, UK, 30 January–1 February 1979; pp. 167–169.
30. Mynett, A.E.; Serman, D.D.; Mei, C.C. Characteristics of Salter's cam for extracting energy from ocean waves. *Appl. Ocean Res.* **1979**, *1*, 13–20. [CrossRef]
31. Serman, D.D.; Mei, C.C. Note on Salter's energy absorber in random waves. *Ocean Eng.* **1980**, *7*, 477–490. [CrossRef]
32. Salter, S. Recent progress on ducks. *IEE Proc. A (Phys. Sci. Meas. Instrum. Manag. Educ. Rev.)* **1980**, *127*, 308–319. [CrossRef]
33. Pecher, A.; Kofoed, J.P.; Larsen, T.; Marchalot, T. Experimental study of the Weptos wave energy converter. In Proceedings of the International Conference on Offshore Mechanics and Arctic Engineering, Rio de Janeiro, Brazil, 1–6 July 2012; pp. 525–534.
34. Zhou, B.-Z.; Li, J.-H.; Zhang, H.-M.; Chen, L.-F.; Wang, L.; Jin, P. Wave extraction and attenuation performance of an Edinburgh Duck wave energy converter. *China Ocean Eng.* **2021**, *35*, 905–913. [CrossRef]
35. Foteinis, S. Wave energy converters in low energy seas: Current state and opportunities. *Renew. Sustain. Energy Rev.* **2022**, *162*, 112448. [CrossRef]
36. Si, Y.; Chen, Z.; Zeng, W.; Sun, J.; Zhang, D.; Ma, X.; Qian, P. The influence of power-take-off control on the dynamic response and power output of combined semi-submersible floating wind turbine and point-absorber wave energy converters. *Ocean Eng.* **2021**, *227*, 108835. [CrossRef]
37. Kamarlouei, M.; Gaspar, J.F.; Calvario, M.; Hallak, T.S.; Mendes, M.J.G.C.; Thiebaut, F.; Guedes Soares, C. Experimental study of wave energy converter arrays adapted to a semi-submersible wind platform. *Renew. Energy* **2022**, *188*, 145–163. [CrossRef]
38. Guo, B.; Wang, T.; Jin, S.; Duan, S.; Yang, K.; Zhao, Y. A Review of Point Absorber Wave Energy Converters. *J. Mar. Sci. Eng.* **2022**, *10*, 1534. [CrossRef]

39. Garcia-Teruel, A.; Forehand, D. A review of geometry optimisation of wave energy converters. *Renew. Sustain. Energy Rev.* **2021**, *139*, 110593. [CrossRef]
40. Aderinto, T.; Li, H. Review on Power Performance and Efficiency of Wave Energy Converters. *Energies* **2019**, *12*, 4329. [CrossRef]
41. Welch, P. The use of fast Fourier transform for the estimation of power spectra: A method based on time averaging over short, modified periodograms. *IEEE Trans. Audio Electroacoust.* **1967**, *15*, 70–73. [CrossRef]